



Advances in Optics and Photonics

When metasurface meets hologram: principle and advances

QIANG JIANG , GUOFAN JIN, AND LIANGCAI CAO *

State Key Laboratory of Precision Measurement Technology and Instruments, Department of Precision Instruments, Tsinghua University, Beijing 100084, China

*Corresponding author: clc@tsinghua.edu.cn

Received January 30, 2019; revised May 31, 2019; accepted June 3, 2019; published August 14, 2019 (Doc. ID 346649)

Holography has numerous applications because of its capability of arbitrary wavefront modulation. Computer-generated holograms (CGHs) take it a big step forward. Conventional holography engineers the wavefront via phase accumulation, suffering from large size, low resolution, and small viewing angle. Metasurfaces, ultrathin two-dimensional metamaterials with subwavelength features, can manipulate the amplitude, phase, and polarization of the light, solving the above issues. In this review, advances of holography, CGH algorithms, and the principles of various metasurfaces are presented. Metasurface holography, realized by encoding the hologram in the metasurface, is investigated. Information multiplexing methods of metasurface holograms, including wavelength-multiplexed, polarization-multiplexed, complex amplitude modulated, nonlinear, and dynamic metasurfaces, are presented. The challenges and outlook of metasurface holograms are discussed. © 2019 Optical Society of America

<https://doi.org/10.1364/AOP.11.000518>

1. Hologram	520
1.1. History and Present of Holography.	520
1.2. Classification of Holograms.	523
1.3. CGH Algorithms	524
1.3a. Basic Theory of Diffraction	524
1.3b. Encoding Methods of Holograms	527
1.3c. 3D Hologram Algorithms	530
2. Metasurface.	534
2.1. Emergence of the Metasurface.	534
2.2. Mechanism of Metasurfaces	535
2.2a. Plasmonic Resonant Phase Type Metasurfaces	535
2.2b. Geometric Phase Type Metasurfaces	537
2.2c. Huygens' Principle-Based Type Metasurfaces	539
2.2d. Propagation Phase Type Metasurfaces	540
2.2e. Circuit Phase Type Metasurfaces	541
2.2f. Nonlinear Metasurfaces	542

3. When Metasurface Meets Hologram	543
3.1. Metasurface Holograms without Multiplexing.	546
3.2. Polarization-Multiplexed Metasurface Holograms	548
3.2a. Linear-Polarization-Multiplexed Metasurfaces	548
3.2b. Circular-Polarization-Multiplexed Metasurfaces	550
3.3. Wavelength-Multiplexed Metasurface Holograms	551
3.3a. Metasurface Based on Multiple Kinds of Meta-Atoms	551
3.3b. Metasurface Based on a Single Kind of Meta-Atom	553
3.4. Complex Amplitude Metasurface Hologram.	553
3.5. Nonlinear Holographic Metasurfaces.	556
3.6. Dynamic Holographic Metasurfaces	557
3.7. Multiple Multiplexing Holographic Metasurfaces	561
4. Conclusions and Perspective	561
Funding	563
Acknowledgment	563
References	564

When metasurface meets hologram: principle and advances

QIANG JIANG, GUOFAN JIN, AND LIANGCAI CAO

1. HOLOGRAM

1.1. History and Present of Holography

The word “hologram” originates from the Greek words “holos” (“whole”) and “gramma” (“message”) since holography records the entire information of a light field, both amplitude and phase. Holography consists of two steps. First, an interference pattern, called the hologram, is recorded. Second, the wavefront representing a three-dimensional (3D) object is reconstructed. In the first step, coherent light is divided into two beams by a beam splitter. One of the two beams illuminates the 3D object and the other one directly illuminates a photographic film. These two fronts then interfere on the photographic film and the intensity of the interference pattern is captured by the film, as shown in Fig. 1(a). In the second step, when the photographic film is illuminated by the same reference wave, the object wavefront is reconstructed. The diffraction wavefront creates a virtual image of the object that appears to be where the original object was, as shown in Fig. 1(b).

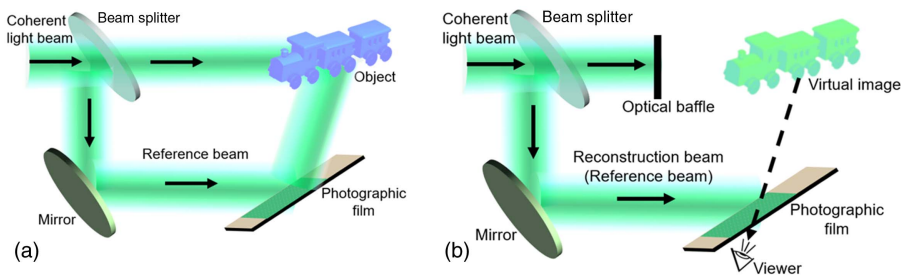
Gabor invented x-ray holography in 1948 for reducing aberrations of electron microscope images [1]. In 1962, Leith and Upatnieks produced the first optical transmission holograms using a laser [2], while Denisyuk produced the first white-light reflection hologram that could be seen under daylight [3]. However, affected by the absorption loss of the recording media, the holographic images were blurry and dull. The performance of the recording materials was improved over the following decades for additional clarity and increased brightness of the projected images. For instance, silver halide emulsion, dichromated gelatin, and photoresist are used for affordable mass production. Photorefractive crystals and polymers behave as reusable real-time recording materials, and the photopolymers are considered to be potential materials for optical holographic storage.

Conventional optical holography requires a complicated system for interference and recording, as well as developing and fixing processes, which are cumbersome. With the availability of computer technology and the development of spatial light modulator (SLM) technology, the wavefront recording and wavefront reconstruction processes of holography can be replaced by numerical calculation. Holograms generated by numerical calculation are called computer-generated holograms (CGHs). In this approach, the object wavefront used to calculate the transmission function of a hologram can be described mathematically by computer [4]. This method eliminates the requirements of real objects for a hologram, making it possible to reconstruct all kinds of fictitious objects, greatly expanding the developments of holographic technology. Figure 2 shows the CGHs of a single point, a slit, and the letters “THU.”

The CGH was first proposed by Kozma and Kelly in 1965 [5]. A hard-clipped matched filter was calculated and written onto a photographic film. This filter could be used as a multi-channel filter bank in a two-dimensional (2D) optical system. Between 1966 and 1980, the basic principles of computer-generated holography and the encoding method were studied. The detour phase hologram, a two-level hologram that was initially applied to image reconstruction by Brown and Lohmann, was widely applied to generating binary computer-generated holograms [6]. The kinoform, a type of

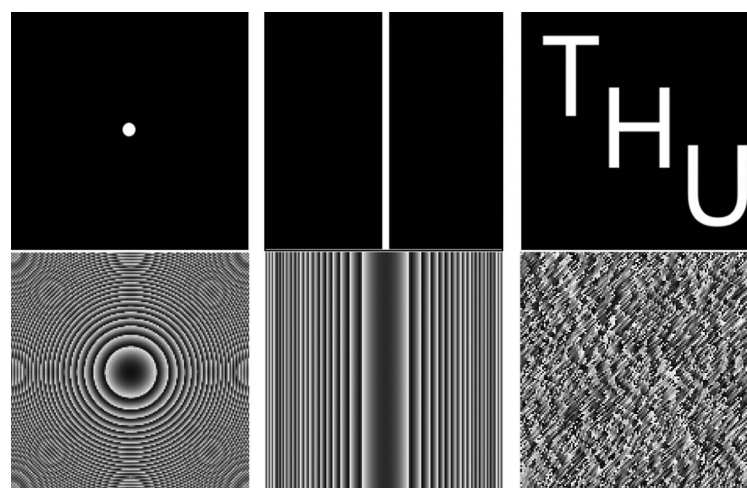
phase-only computer-generated hologram that uses the relief images recorded on film to record the phase variations of the complex wavefront calculated by the computer, was also proposed during this period [7]. In the next two decades, electro-holography and 3D CGH algorithms were developed. The first real-time 3D hologram was realized by using a SLM [8]. From 2001 to 2010, typical devices such as liquid crystal on silicon (LCoS) devices and digital micro-mirror devices (DMDs) [9] were employed to encode computer-generated holograms. Meanwhile, many methods for improving image quality have been studied. Algorithms and models such as the angular spectrum [10], analytic [11], and polygon-based models [12] have been proposed. With the development of hardware technology, field-programmable gate array (FPGA) devices and graphics processing units (GPUs) were used to speed up the operation of the programs [13,14]. The information capacity of spatial signals in holography can be described by the space-bandwidth product (SBP), which is determined as the product of the physical dimension and the corresponding 2D bandwidth of the SLM. The SBP limits the viewing angle and the viewing window [15]. In the next stage, many methods have been proposed to improve the SBP [16–18]. In 2015, a threefold increase in SBP of a single SLM using high-order diffraction guided by a holographic optical element was realized [19]. Research on holographic algorithms continues to progress. Shading CGH [20] and the ray-sampling [21], ray-tracing [22], and angular tilting models [23] were proposed

Figure 1



(a) Recording and (b) reconstruction in off-axis optical holography.

Figure 2



Single point, slit, the letters “THU,” and their corresponding computer-generated holograms.

during this time. The main purpose of the algorithms based on these models is to improve the overall 3D effect of CGH, including lighting, accommodation cue, occlusion, and rendering. Table 1 lists some selected CGH research milestones.

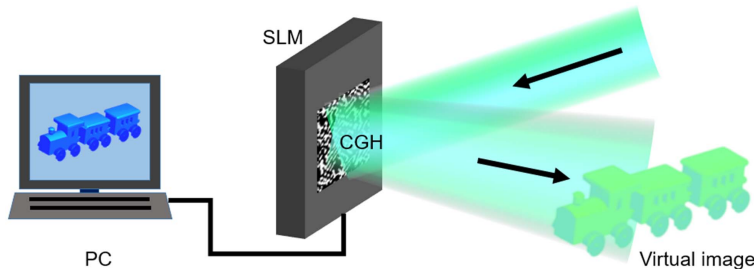
The SLM is a general term that describes a device that consists of many repeated units (pixels), in which each unit modulates the amplitude, phase, or polarization of light waves independently in space and time. SLMs can be classified into two types based on the addressing mode, which refers to the type of input signal that controls the optical properties. For electrically addressed SLMs, an electric signal generated by a computer is used to change a variable associated with the incident light beam. The pixel pitch of these SLMs is between 3.5 and 20 μm . For optically addressed SLMs, an optical signal is used to change a variable associated with the incident light beam. The information is written to materials whose optical properties vary with the incident light. Photo-refractive or photo-chromic materials can be modulated by a laser beam or an optical image from a display device. Besides SLMs, dielectric gratings [24,36] and optical antennas [7] are also employed as holograms for wavefront modulation.

By utilizing a reference beam, the holograms encoded in SLMs can be read out, as shown in Fig. 3. However, the viewing angle of the reconstructed images is limited

Table 1. Selected CGH Research Milestones

Years	Features	Main Methods	Reference
1966–1980	•Basic principles of CGH •Encoding method	Binary Fourier hologram	[6]
		Detour phase hologram	[4]
	•Electro-holography •3D CGH algorithms	Point source model	[24]
		Phase-only hologram	[7]
		Sampled Fourier hologram	[25]
		CGH of tilted planes	[26]
		Electro-holography	[27]
1981–2000	•Look-up table method	Look-up table method	[28]
		Phase-added stereogram	[29]
	•Quality improvements •Diffraction efficiency increasing	Integral holography	[30]
		DMD-based CGH	[9]
		Angular spectrum model	[31]
2001–2010	•Hardware acceleration	GPU-based CGH	[13]
		Polygon based model	[11,12]
	•Bandwidth product expanding •Advanced algorithms for CGH	Ray-sampling model	[21]
		Shading CGH	[20]
		Ray-tracing model	[22,32]
		Angular tilting model	[23]
		Table screen CGH	[18]
2011–present		Stereogram based algorithm	[33–35]

Figure 3



Schematic of hologram reconstruction in computer-generated holography.

by the pixel pitch of the SLMs. The maximum diffraction angle φ_v , which is half of the viewing angle, can be calculated for the pixel pitch p :

$$\varphi_v = \sin^{-1} \left(\frac{\lambda}{2p} \right). \quad (1)$$

From Eq. (1), it is clear the pixel pitch of the SLM should be sufficiently smaller than the wavelength λ so as to display 3D images with a large viewing angle. Considering even the finest 8K SLM with a pixel pitch of 3.5 μm as an example, in the visible range, the viewing angle is only about 10°. With the demands of further expanding our perception and enriching our visual information, 3D display technology that creates virtual objects and even displays them with the real objects has been developed. The current mainstream of 3D display technology includes mainly light field 3D display, volumetric 3D display, and CGH display. Among them, CGH display takes advantage of the precise reappearance of depth information, resulting in a realistic reconstructed scene with an immersive environment for viewers, which solves the convergence-accommodation problem and presents a virtual environment without causing dizziness [37]. This advantage makes the holographic display predominant over peer 3D display technologies. Nevertheless, a common issue for all holographic display devices is that they must simultaneously possess a narrow pixel pitch for a wide viewing-zone angle and many pixels for a large-enough viewing window.

1.2. Classification of Holograms

Holograms can be classified into several types by different aspects.

- (1) According to the relative positions of the reconstructed and conjugate images.
 - In-line. A plane wave illuminates a particle or a particle field. The diffracted light acts as an object beam, which is able to interfere with the undisturbed wave.
 - Off-axis. The object being illuminated reflects part of the light onto a film, which is simultaneously exposed to a reference beam.
- (2) According to the relative positions of the illumination and reconstruction waves.
 - Transmission type. The illumination wave and the reconstruction wave are located on opposite sides of the SLM.
 - Reflection type. The illumination wave and the reconstruction wave are located on the same side of the SLM.
- (3) According to the wavelength of illumination light.
 - Monochromatic. The object is illuminated by a monochromatic illumination wave and the virtual image is reconstructed under the same illumination wave.
 - Rainbow. A type of hologram designed to be viewed under white-light illumination, rather than laser light. The rainbow holography recording process uses a horizontal slit to eliminate vertical parallax in the output image, greatly reducing spectral blur while preserving 3D for most observers. A viewer moving up or down in front of a rainbow hologram sees changing spectral colors rather than different vertical perspectives.
- (4) According to the modulation.
 - Amplitude holograms are made up of an interference pattern that results in a variation of either the transmission coefficient or the reflection coefficient in the

recording plane. The amplitude of the reference beam is modulated by the hologram, and the transmittance phase is constant.

- Phase holograms encode the information using variation in the refractive index or in the thickness of the photographic film, which causes a modulation of the phase of the reference beam during reconstruction. The transmittance amplitude is unity.
- Complex amplitude. The material or device modulates both the phase and amplitude of an incoming wavefront.

(5) According to the reconstruction distances of the holograms.

- The image hologram is formed by placing a photographic film near the location of the real image formed by a lens. The reconstructed image is located on the hologram plane.
- Fresnel hologram. The hologram is recorded on the plane located in the Fresnel zone of the object's diffracted light field. The Fresnel approximation is more accurate in the near field.
- Fourier transform (FT) hologram. The reconstructed image is located in the far field. This is usually achieved by using the Fourier transforming properties of a positive lens for reconstruction. Thus, there are two steps in this process: computing the light field in the distant observer plane, and then Fourier transforming this field back to the lens plane.

1.3. CGH Algorithms

Generation of a CGH consists of three main steps.

- (1) Calculating. Calculating the complex fields that the object wave will produce on the hologram plane, which could be the discrete Fourier transform (DFT) of the complex amplitude of points in the object plane.
- (2) Encoding. Choosing a suitable representation of the complex fields in the hologram plane. The calculated complex (both amplitude and phase) discrete sample values of the DFT are usually used to produce a hologram that will reconstruct the object when illuminated by an appropriate laser source.
- (3) Uploading. Transferring the encoded representation of the complex fields to a transparency by printing or plotting or onto a SLM.

There are many different methods for calculating the interference pattern for a computer-generated hologram. In computational techniques, the reported algorithms can be categorized by two main concepts: FT holograms (cell oriented) [23,38,39–41] and point-source holograms (point oriented) [10,24,28,42–44].

1.3a. Basic Theory of Diffraction

The basic problem in diffraction theory is to analyze the complex amplitude on the observation plane after the light emitted by the light source is scattered by the diffraction object. The basic idea of diffraction is the Huygens–Fresnel theory, which treats the light disturbance at a point P as arising from the superposition of secondary waves that proceed from a surface situated between this point P and the light source. By using Kirchhoff boundary conditions and Green's theorem, Kirchhoff's diffraction theory is established. By modifying the Green's function belonging to the surface surrounding the point P, the Rayleigh–Sommerfeld diffraction integral of the first kind and second kind are proposed. The difference between the Rayleigh–Sommerfeld and Fresnel–Kirchhoff formalism is the inclination factor, and is usually immaterial because the inclination factor is approximated by unity. However, when

this approximation is not valid, the Fresnel–Kirchhoff formalism can lead to unrealistic results [45].

In this section, the most widely used methods of diffraction calculation are discussed.

(a) Rayleigh–Sommerfeld diffraction. Figure 4 shows a holographic reconstruction system. Assuming $t(x,y)$ is the transmission function of the hologram, $u(x,y)$ is the complex amplitude of the incident light on the hologram plane, the complex amplitude $u_1(x_1,y_1)$ on the image plane can be calculated based on the Rayleigh–Sommerfeld diffraction integral [46],

$$u_1(x_1,y_1) = \iint u(x,y)t(x,y) \frac{\exp(jkr)}{2\pi r^3} z_d(jkr - 1) dx dy, \quad (2)$$

where r is the distance between the sampling points in the hologram plane and in the image plane:

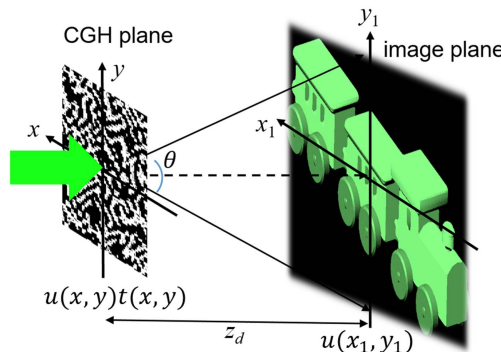
$$r = \sqrt{(x_1 - x)^2 + (y_1 - y)^2 + z_d^2}. \quad (3)$$

The Rayleigh–Sommerfeld diffraction integral is the most accurate calculation method under scalar diffraction theory. It does not use any physical approximation. Normally, there is no analytical solution for this diffraction integral. It can be solved only by a numerical method. The simplest method is to convert the integral into a sum, but the summation operation requires a lot of time. This is inappropriate for CGH algorithms that require repeated iterations between the hologram plane and image plane. Further, Eq. (2) can also be regarded as a convolution of two functions, which can be calculated by fast Fourier transformation (FFT) [47]. However, it requires the same sampling interval on the hologram and the image plane.

(b) Fresnel diffraction. The integrand function in the Rayleigh–Sommerfeld diffraction integral is complex and the calculation is time consuming. Therefore, the Rayleigh–Sommerfeld diffraction integral is often approximated according to the actual diffraction problem.

Some approximation can be done to Eq. (2). Usually, λ and the size of the hologram are much smaller than r . Thus, $jkr - 1 \approx jkr$. Besides, in the amplitude term, the amplitude change caused by the change of r is negligible; thus, $r \approx zd$, while the phase change caused by the change of r cannot be neglected directly. The binomial expansion of Eq. (3) can be expressed as

Figure 4



Holographic reconstruction through Rayleigh–Sommerfeld diffraction.

$$r = z_d \left\{ 1 + \frac{1}{2} \left[\frac{(x_1 - x)^2 + (y_1 - y)^2}{z_d^2} \right] - \frac{1}{8} \left[\frac{(x_1 - x)^2 + (y_1 - y)^2}{z_d^2} \right]^2 + \dots \right\}. \quad (4)$$

When the reconstruction distance z_d is large enough to make the contribution of the third term to the phase far less than π , Eq. (2) can be further approximated as

$$u_1(x_1, y_1) = \frac{\exp(jkz_d)}{j\lambda z_d} \iint u(x, y) t(x, y) \exp \left\{ \frac{jk}{2z_d} [(x_1 - x)^2 + (y_1 - y)^2] \right\} dx dy, \quad (5a)$$

$$\frac{k}{8z_d^3} [(x_1 - x)^2 + (y_1 - y)^2]_{\max}^2 \ll \pi. \quad (5b)$$

Under the Fresnel approximation, the contribution of any point on the hologram to the complex amplitude at any point on the output plane depends only on the coordinate difference between the two points, which shows that the holographic reconstruction system under the Fresnel approximation has spatial invariance.

(c) Fraunhofer diffraction. By increasing z_d , the reconstructed field described in Eq. (2) can be further approximated as

$$u_1(x_1, y_1) = \frac{\exp(jkz_d)}{j\lambda z_d} \exp \left[\frac{jk}{2z_d} (x_1^2 + y_1^2) \right] \iint u(x, y) t(x, y) \exp \left[\frac{-jk}{z_d} (xx_1 + yy_1) \right] dx dy, \quad (6a)$$

$$k \frac{(x^2 + y^2)_{\max}}{2z_d} \ll \pi. \quad (6b)$$

Under the Fraunhofer condition, the complex amplitude distribution of the reconstructed image can be obtained by the FT of the hologram. Comparison of Eqs. (5b) and (6b) shows that the requirement for the distance z in the Fraunhofer region of the hologram is much more stringent than that in the Fresnel region. The Fresnel hologram can be reconstructed by a lensless optical system. However, Fraunhofer holograms often require lenses for reconstruction.

(d) Angular spectrum theory of plane waves: The scalar diffraction theory can also be expressed in the framework of linear invariant system theory. Here we introduce an approach to the diffraction problem that is more consistent with linear systems theory and obtains the corresponding transfer function in spatial frequency space. The present approach is known as the angular spectrum method for the description of the diffraction problem [48].

Assuming the complex field in the hologram plane is $h(x, y)$, the spatial spectrum, defined as the complex amplitude density of a plane wave component with a spatial frequency of (u, v) , can be expressed as

$$H(u, v) = \int_{-\infty}^{\infty} \int h(x, y) \exp[-j2\pi(f_x x + f_y y)] dx dy. \quad (7)$$

In this formalism, $h(x, y)$ is decomposed into a series of 3D plane waves propagating in different directions. The spatial frequency (u, v, w) determines the propagation direction of each plane wave. As shown in Fig. 5, the spatial frequency can be expressed by the direction cosine (α, β, γ) :

$$u = \alpha/\lambda; \quad v = \beta/\lambda; \quad w = \gamma/\lambda, \quad (8)$$

$$w = \frac{1}{\lambda} \sqrt{1 - \lambda^2 u^2 - \lambda^2 v^2}. \quad (9)$$

When the plane wave propagates in free space, the shape of the wavefront does not change; only a phase delay related to the propagation distance is generated. The spatial spectrum $E(u, v)$ in the image plane can be obtained from $H(u, v)$ after propagation for a distance of z :

$$E(u, v) = H(u, v) \exp \left[jkz \sqrt{1 - \lambda^2 u^2 - \lambda^2 v^2} \right]. \quad (10)$$

Then, the complex field $e(x_1, y_1)$ in the image plane can be obtained by using the inverse Fourier transform (IFT).

1.3b. Encoding Methods of Holograms

In computational holography, the input spatial complex signal is recorded in an intermediate medium, and finally the complex signal is reproduced in an optical form. Similar to a communication system, the process of transforming a spatial complex signal into a CGH wavefront modulation function is called the encoding process. The choice of encoding method should match the modulation type of hologram display medium. A brief description is given of some of the main encoding methods, which include detour phase, modified off-axis reference beam, and phase-only CGH.

(a) Detour phase. Before gray-tone plotters and SLMs were available, the first quality image was reconstructed from a binary, amplitude-only hologram, that is the Fourier-type detour-phase hologram, which was invented by Brown and Lohmann [6].

Figure 6 shows the setup for reconstructing a Fourier hologram through a FT lens of focal length f . The hologram is composed of $M \times N$ hologram cells. Each cell of size $d \times d$ contains a rectangular window with an area of $w_{mn} \times l_{mn}$. The offset distance from the center of the window to the center of the unit cell is p_{mn} . The complex optical field $u(x, y)$ of the reconstructed image and the complex field $h(x, y)$ at the hologram can be controlled by $w_{mn} \times l_{mn}$ and p_{mn} , respectively. Assuming that the (m, n) th cell is located at (x_{mn}, y_{mn}) on the hologram plane, $u(x, y)$ can be written as a DFT as shown in Eq. (11) [49]:

Figure 5

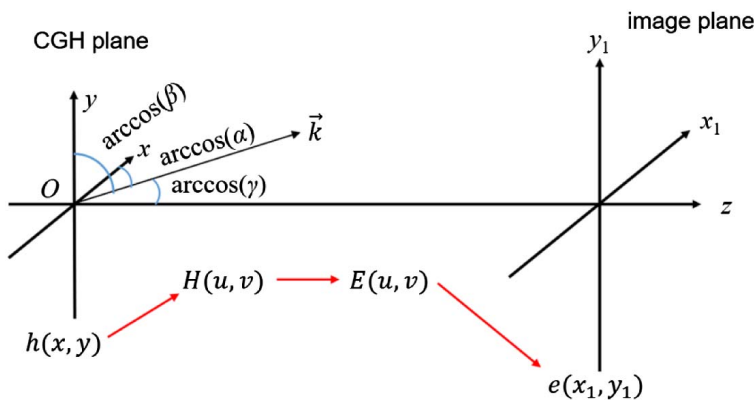


Illustration of the angular spectrum theory.

$$\begin{aligned}
u(x, y) &= \frac{jk_0}{2\pi f} \mathcal{F}[\exp(-jk_x x) h(x, y)]_{k_x = \frac{k_0 x}{f}, k_y = \frac{k_0 y}{f}} \\
&= \frac{jk_0}{2\pi f} \sum_{m=0}^{M-1} \sum_{n=0}^{N-1} w_{mn} l_{mn} \operatorname{sinc}\left[\frac{w_{mn} k_0}{2\pi f} \left(x - \frac{2\pi f}{\Delta x k_0}\right)\right] \operatorname{sinc}\left(\frac{l_{mn} k_0}{2\pi f} y\right) \\
&\quad \times \exp\left[-j\frac{k_0}{f} (xx_{mn} + yy_{mn})\right] \\
&\quad \times \exp\left(-j\frac{k_0}{f} p_{mn} x\right) \exp(-jk_x p_{mn}) \exp(-jk_x x_{mn}). \tag{11}
\end{aligned}$$

(b) Modified off-axis reference beam CGH. By using a reference light wave, the complex amplitude on the hologram plane can be transformed into a real nonnegative discrete sampling function, that is, it imitates the method of optical off-axis hologram formation. The transmission function of the off-axis optical hologram can be expressed as

$$\begin{aligned}
h(x, y) &= |O(x, y) + R(x, y)|^2 \\
&= |A(x, y) \exp[j\varphi(x, y)] + R(x, y)|^2 \\
&= |R(x, y)|^2 + |A(x, y)|^2 + 2R(x, y)A(x, y) \cos[2\pi\alpha x - \varphi(x, y)], \tag{12}
\end{aligned}$$

where $O(x, y)$ and $R(x, y)$ are the complex amplitudes of the object wave and reference wave, respectively, and $A(x, y)$ and $\varphi(x, y)$ are the amplitude and phase of the object wave, respectively. $|R(x, y)|^2$ and $|A(x, y)|^2$ make $h(x, y)$ a real nonnegative function, while $2R(x, y)A(x, y) \cos[2\pi\alpha x - \varphi(x, y)]$ provide all the information about the object. However, the first two items enlarge the bandwidth of the hologram recording and result in redundant diffraction images during reconstruction. In the generation of computer-generated holograms, the first two items can be replaced by other offset components. Assuming that $R(x, y) = 1$, $|A(x, y)|_{\max} = 1$, Eq. (12) can be

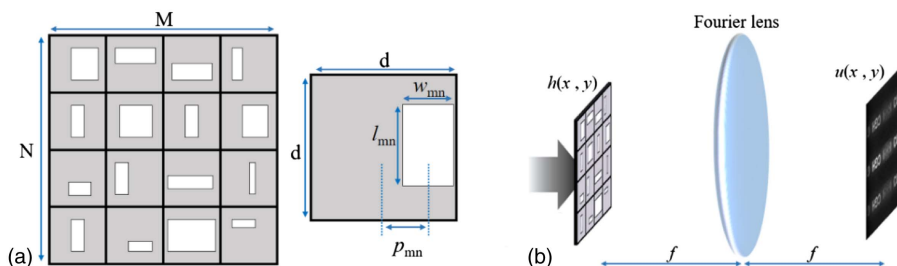
$$h(x, y) = 0.5\{1 + A(x, y) \cos[2\pi\alpha x - \varphi(x, y)]\}. \tag{13}$$

This simplification, first proposed by Burch in 1967 [50], reduces the total number of sampling points to 25% compared to that of the method expressed by Eq. (12).

In Huang's method [51], the transmission function $h(x, y)$ is expressed as

$$h(x, y) = 0.5A(x, y)\{1 + \cos[2\pi\alpha x - \varphi(x, y)]\}. \tag{14}$$

Figure 6



(a) Encoding using the detour method. (b) The setup for reconstructing a Fourier hologram with detour encoding CGH.

Compared to Burch's method, Huang's method does not reduce the number of samples, and the nonlinear effect of the recording medium has much influence on the hologram. However, the contrast of the reconstructed images is higher than that of Burch's method, which reduces the requirement for the accuracy of the display - recording device, and film exposure and development.

In another method proposed by Lee in 1970 [25], as is shown in Eq. (15), the complex value of a sampling point on a hologram can be decomposed into four orthogonal components, all of which are real nonnegative functions:

$$A(u, v) | \exp[j\varphi(u, v)] = A_1(u, v) - A_3(u, v) + jA_2(u, v) - jA_4(u, v), \quad (15a)$$

$$A_1(u, v) = \begin{cases} |\mathbf{A}(u, v)| \cos[\varphi(u, v)], & \cos[\varphi(u, v)] > 0 \\ 0, & \text{otherwise} \end{cases}, \quad (15b)$$

$$A_2(u, v) = A_1(u, v) - |\mathbf{A}(u, v)| \cos[\varphi(u, v)], \quad (15c)$$

$$A_3(u, v) = \begin{cases} |\mathbf{A}(u, v)| \sin[\varphi(u, v)], & \sin[\varphi(u, v)] > 0 \\ 0, & \text{otherwise} \end{cases}, \quad (15d)$$

$$A_4(u, v) = A_2(u, v) - |\mathbf{A}(u, v)| \sin[\varphi(u, v)]. \quad (15e)$$

Compared to Burch's method and Huang's method, Lee's method has a higher requirement for sampling number and calculation amount. However, because phase coding is not needed, phase quantization errors will not be introduced to affect the accuracy of the reconstructed image.

(c) Phase-only hologram. Although the d etour-phase hologram can represent the phase as well as the modulus of a sampled complex hologram, its diffraction efficiency is relatively low. To achieve high diffraction efficiency, the kinoform hologram, which is based on the scheme of Fourier holography, was proposed. By associating a random-phase mask with the object pattern, the energy can be distributed approximately uniformly across a wide spectrum; therefore, the modulus $a(x, y)$ becomes relatively unimportant and can be ignored. Thus, in the formation of a Fourier hologram $h(x, y) = a(x, y) \exp[-j\phi(x, y)]$, it is required only to extract the phase $\phi(x, y)$. A gray-scale pattern whose gray level is proportional to $\phi(x, y)$ can be displayed on a phase-only SLM or printed on a photographic film.

The diffraction efficiency of the kinoform hologram is greater than that of the detour-phase hologram, and may even approach 100%. However, the resulting image reconstructed from the kinoform hologram is usually noisy. Owing to the features of high diffraction efficiency, ease of fabrication, and flexibility for optical information processing, phase-only CGH has attracted much attention. Researchers have proposed a number of optimization methods to improve the quality of reconstructed images, including iterative Fourier or Fresnel transform algorithms (IFTA) [52,53], simulated annealing (SA) [54], the genetic algorithm (GA) [55–57], the Gerchberg–Saxton algorithm (GSA) [58–61], the Yang–Gu algorithm [62], and the input–output algorithm [63].

Among all these algorithms, the GSA is the most commonly used algorithm for phase-only Fourier holograms. The GSA is an iterative algorithm that employs FFT for retrieving the phase of light distribution. In holography, the GSA is widely used

to obtain high-quality phase-only holograms. A phase-only function at the input plane is retrieved while assigning a given target image at the output plane. The final phase-only hologram can be obtained by iteratively applying the FT and IFT and setting the necessary constraints on the input and output planes, until the error between the original target and the iteratively reconstructed images converge. Under the illumination of a plane wave, the process can be simplified as follows, as shown in Fig. 7.

- (1) Replace the phase in the image plane by a random phase matrix φ_0 , while the amplitude A_0 remains unchanged.
- (2) The field propagates from the image plane to the object plane. The amplitude A_1 is discarded and the phase φ_1 is retained.
- (3) The optical field E_2 propagates from the object plane to the image plane.
- (4) The amplitude A_3 of the resulting reconstructed image is compared with the expected one A_0 . The decision to terminate or continue the process is made by the correlation between A_3 and A_0 .
- (5) The phase φ_3 of the reconstructed image is combined with the amplitude A_0 obtained from the object. The process is then repeated from step (2).

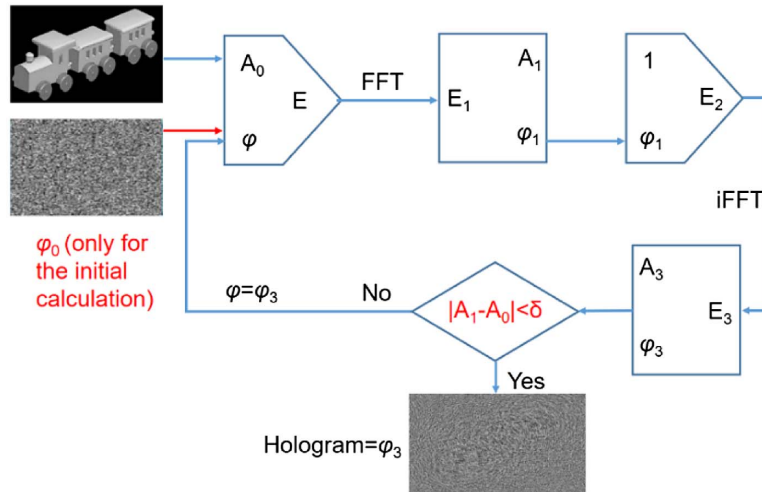
1.3c. 3D Hologram Algorithms

In holography, the complex field of light from the scene is calculated in the hologram plane by diffraction theory using the digital data of the virtual 3D scene. The complex amplitude in the hologram plane $h(x, y)$ can be described by the Huygens–Fresnel principle. According to the classification of primitives, a 3D CGH technology can be divided into point-, polygon-, layer-, and stereogram-based methods.

(a) Point-based algorithm. In the point-based approach, the 3D scene is represented as aggregated point sources [20], as shown in Fig. 8. Assuming that the coordinates of points on the CGH plane are (x, y, z) and the coordinates of points representing the object are (x_m, y_m, z_m) , the distance r_m between points on the object and points on the CGH plane can be expressed as

$$r_m = \sqrt{(x_m - x)^2 + (y_m - y)^2 + (z_m - z)^2}. \quad (16)$$

Figure 7



Flow chart of the GSA.

Then the optical field for the entire 3D scene is simply given by

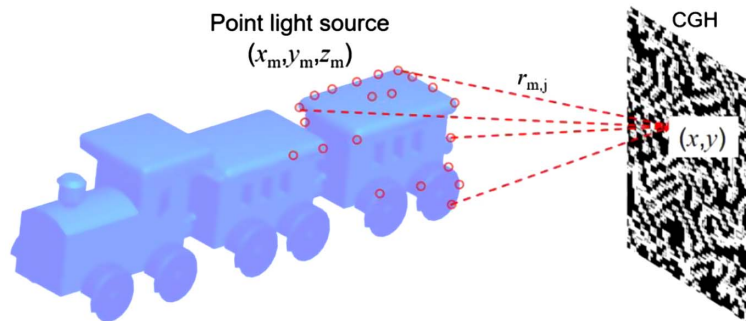
$$h(x,y) = \sum_m \frac{A_m}{r_m} \exp\left(-\frac{j2\pi}{\lambda} r_m\right). \quad (17)$$

Here, A_m is the light intensity.

(b) Polygon-based algorithm. The polygon-based method represents the 3D scene as aggregates of small planar polygons, as shown in Fig. 9. The optical field of each polygon facet is calculated and accumulated in the hologram plane to obtain the final hologram of the 3D scene. The calculation of the optical field of the polygon facet is performed by finding the relationship between the angular spectra represented in the hologram plane and in the local plane containing the polygon facet [64].

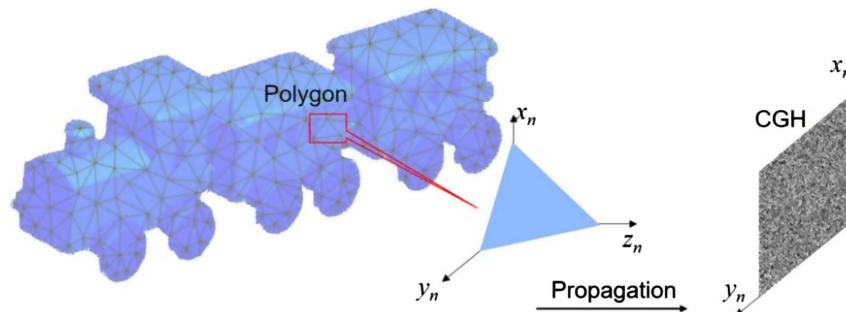
There are two approaches according to the way the local angular spectrum is obtained [65]. In one approach, known as the FFT-based method [12], the local angular spectrum is obtained in discrete form by taking the discrete Fourier transform of the triangular facet in the local plane. In another approach, known as the “fully analytic method,” the local angular spectrum is related to the analytic formula of the angular spectrum of a reference triangle [66,67]. In either approach, the most essential and significant operation is the coordinate rotation in the Fourier domain. This will be described as follows. For the detailed operations of these two approaches, one can refer to the current works [31,64,67].

Figure 8



Point-based method for calculating the hologram of a 3D scene.

Figure 9



Schematic of polygon-based method for calculating a hologram.

Suppose that global coordinates (x, y, z) and local coordinates (x_n, y_n, z_n) are defined such that the hologram plane is at $z = 0$ and the polygon is at the $z_n = 0$ plane. The Fourier transform of the i th surface wavefront distribution is

$$H_i(u_i, v_i) = F[h_i(x_i, y_i)]. \quad (18)$$

The diffracted field from a tilted polygon is obtained by applying angular spectrum-based diffraction to the source or target plane in the frequency domain. This is followed by transformation between local and global coordinates. Finally, the diffracted field in the spatial domain is obtained using the inverse FFT. The diffracted field in the frequency domain, $U(u, v)$, is transformed by the rotation matrix M . The relation of the diffracted field in the frequency domain before and after rotation is as follows:

$$U(u, v) = U' \left(a(u, v) - \frac{1}{\lambda}, \beta(u, v) - \frac{1}{\lambda} \right), \quad (19)$$

where

$$U(u, v) = \mathcal{F}[a(x, y)], \quad (20a)$$

$$U'(u, v) = \mathcal{F}[a(x', y')], \quad (20b)$$

$$M = \begin{bmatrix} a_{11} & a_{12} & a_{13} \\ a_{21} & a_{22} & a_{23} \\ a_{31} & a_{32} & a_{33} \end{bmatrix}, \quad (20c)$$

$$a(u, v) = a_{11}u + a_{12}v + a_{13}w(u, v), \quad (20d)$$

$$\beta(u, v) = a_{21}u + a_{22}v + a_{23}w(u, v), \quad (20e)$$

$$w(u, v) = \sqrt{\lambda^{-2} - u^2 - v^2}. \quad (20f)$$

Therefore, the optical field in hologram plane is given by $h(x, y) = \mathcal{F}^{-1}[U(u, v)]$.

(c) Layer-based algorithm. The layer-based method slices the 3D scene into multiple parallel layers according to the depth information. The hologram is obtained by numerically propagating individual layers to the hologram plane and accumulating them. This method greatly reduces the calculation load of the 3D scene. One of its significant features is the trade-off between resolution of accommodation cue and resultant calculation speed. The actual calculation speed has been proved to be high while the image quality remains high. The calculation speed could be further increased according to different approaches, such as the region fraction [68], angular spectrum [39], and inverse Fresnel diffraction approaches [35]. As is depicted in Fig. 10, the layered angular spectrum method is taken as an example to introduce the layer-based algorithm. Let $e_i(x, y, z = z_i)$ be the intensity distribution of the object slice at the $z = z_i$ plane. The optical field at the $z = z_i$ plane is calculated by using angular spectrum diffraction [39],

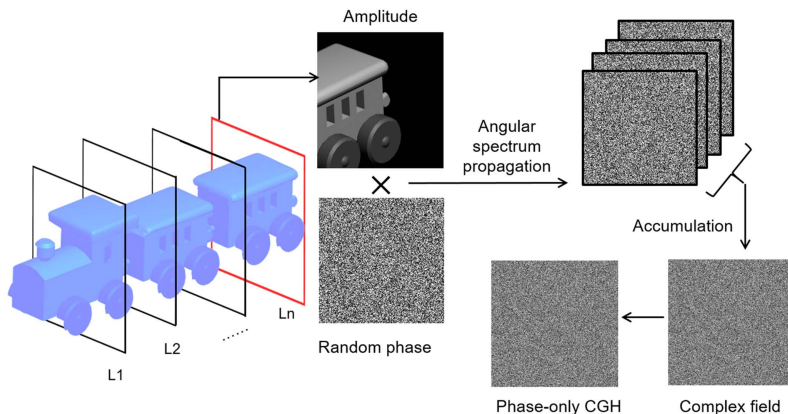
$$h(x, y) = \sum_n \iint E_i(u, v) \exp(jkd\sqrt{1 - \lambda^2 u^2 - \lambda^2 v^2}) \exp[j2\pi(ux + vy)] du dv, \quad (21)$$

where $E_i(u, v) = \iint e_i(x, y) \exp[-j2\pi(ux + vy)] dx dy$.

(d) Stereogram-based algorithm. Stereogram-based algorithms spatially multiplex 2D parallax views of the 3D scene, taking advantage of computer graphics rendering techniques in the parallax view rendering processes [33]. During calculation, the computer-generated hologram is spatially segmented into multiple holographic elements (hogels), and the parallax views are captured by perspective projections from the corresponding viewpoints. Hence, the view-dependent properties can be provided with the help of the multi-viewpoint rendering process. Since each hogel corresponds to only one 2D parallax view in the stereogram-based algorithm, the depth performance would be affected during optical reconstruction, especially the accommodation cue. Recently, a fully computed holographic stereogram was developed to improve the depth performance, which integrated the stereogram-based and physically based algorithm to provide accurate depth information [34]. Inverse Fresnel diffraction with layer-based processing was also implemented in the calculation of the fully computed holographic stereogram to improve the computational efficiency [35].

A diagram of the computed holographic stereogram is shown in Fig. 11. The hologram is spatially partitioned into a grid of hogels. For each hogel, a viewing frustum is

Figure 10



Layer-based angular spectrum method for phase-only hologram. Adapted from [39].

Figure 11

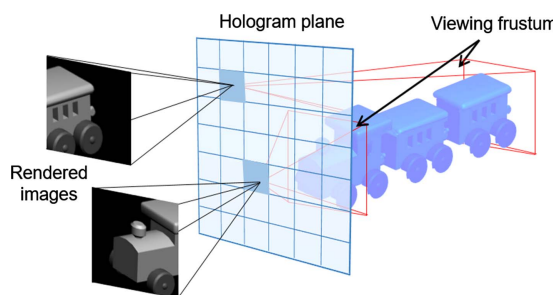


Diagram of the computed holographic stereogram. Adapted from [34].

employed to perform the perspective projection. Several rendered images were used to provide information pertaining to all the object points that have contributions to the corresponding hogel.

2. METASURFACE

2.1. Emergence of the Metasurface

Phase is a basic physical parameter of electromagnetic waves. Traditional optical components that control light propagation based on phase changes, such as prism and lens, which are first-generation optical components, modify phase by accumulating optical paths under the restricted Snell's law. Limited by the refractive index of natural materials, the first generation of optical components have the characteristics of large volume, high quality, and simple function. Diffractive optical elements (DOEs), the second generation of optical components, have made great strides in reducing size, weight, and cost [28]. The DOE has abandoned the redundant 2π phase, making it possible to modulate the phase of the incident light by a thin relief microstructure etched into the DOE substrate. However, with the trend of miniaturization and integration of optoelectronic devices, new structures and mechanisms for wavefront modulation are still imperative, especially in solving the problems of the small field of view of DOEs, and the large aberrations induced by DOEs.

Metamaterials are engineered to have properties that do not exist in naturally occurring materials. They are composed of assemblies of multiple repeating units at the subwavelength scale. The precise geometry, size, orientation, and arrangement of the units give them unique properties for manipulating electromagnetic waves. Relying on such artificial materials, properties such as negative refraction [69] and applications such as superlenses, superresolution [70], and highly directional antennas became possible [71]. Typical metamaterials, including left-handed materials, photonic crystals, and magnetic metamaterials, interact with electromagnetic waves based on their effective refractive index, which modifies the phase by accumulating optical path length. 3D bulk structures are constrained to strict requirements for manufacturing technology. Bulk metamaterials have large dispersion, making them sensitive to the operating wavelength, and it is difficult to achieve broadband operation. In the visible region, the intrinsic absorption loss inside the metamaterials is not negligible. All these challenges have hindered the engineering of metamaterials.

The applications of dimensionality reduction from 3D bulk structure to 2D structure overcome the disadvantages of metamaterials. Recently, metasurfaces, characterized as a kind of 2D metamaterial with ultrathin thickness of the order of wavelength, benefiting from simplified fabrication processes, have been widely adopted to manipulate electromagnetic waves with reduced absorption loss [72–76]. The novel mechanism of metal metasurfaces can be illustrated as a strong interaction between the electromagnetic waves and the electrons in the metal [77,78]. Arbitrary manipulation of amplitude, phase, and polarization of the local field can be achieved on the subwavelength scale by designing the shape of each unit cell. In this way, a phase change is introduced by a phase discontinuity under the general Snell's law, which was proposed by Capasso's group in 2011, rather than by optical path length accumulation [79]. Metasurfaces have evolved into a relatively independent subject, as well as intermingling with surface plasma optics and nonlinear optics. Compared with traditional optical elements, DOEs, and bulk metamaterials, metasurfaces have the following five prominent advantages.

- (1) Ultrathin and low absorption loss. Metasurfaces manipulate the incident light below the wavelength scale, which significantly reduces the loss caused by light propagation in the medium.

- (2) Pixel at a subwavelength size. This provides high resolution in optical field manipulation and avoids the crosstalk caused by the undesired multistage diffraction of DOEs.
- (3) Broadband. With carefully designed unit shape, metasurfaces can operate over a wide range of wavelengths, over which there is weak dispersion.
- (4) Ease of fabrication. A metasurface consisting of 2D arrays of plasmonic or dielectric nanostructures in thin films can be fabricated by conventional surface-lithography techniques, such as photolithography, electron-beam lithography (EBL), focused ion beam (FIB) milling, and nanoimprinting. The Institute of Photoelectric Technology of the Chinese Academy of Sciences has realized batch production by using surface plasma resonance lithography [80].
- (5) Flexible design. Each unit of the metasurface can tailor the light beam independently without crosstalk. Even if there are some defects in a few units, it would not affect the overall function of the surface. As a result of the above advantages, metasurfaces are widely used in focusing [81–85], information processing [86,87], cloaking [88,89], nonlinear converters [90], holograms [91–93], spin-controlled photonics [94,95], vortex generation [96,97], spectrometers [98,99], biological imaging [100], etc. Metasurfaces are expected to be the next generation of optical elements for manipulating optical fields, in place of traditional lenses, DOEs, and 3D bulk metamaterials.

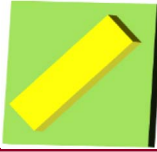
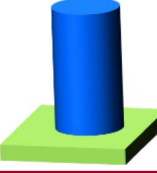
2.2. Mechanism of Metasurfaces

Metasurfaces manipulate electromagnetic waves by using different unit structures within the same metasurface. The abrupt phase change can be customized by varying the geometric parameters of the unit. Several excellent reviews on the recent developments of metasurfaces have discussed the mechanism of different kinds of metasurface in detail [101–105]. From the perspective of the frequency of the output light, we divide the metasurfaces under investigation at present into two types, linear metasurfaces and nonlinear metasurfaces. In linear metasurfaces, the wavefront is manipulated by changing the spatial amplitude and phase profiles of the existing light. The superposition principle is valid for linear metasurfaces. Linear metasurfaces can be classified according to the working mechanism, as resonant phase type, geometric phase type, Huygens principle type, transmission phase type, and circuit phase type, as shown in Table 2 [106–115]. In the nonlinear case, light is directly generated at new frequencies with the desired wavefront by using nonlinear optical materials.

2.2a. Plasmonic Resonant Phase Type Metasurfaces

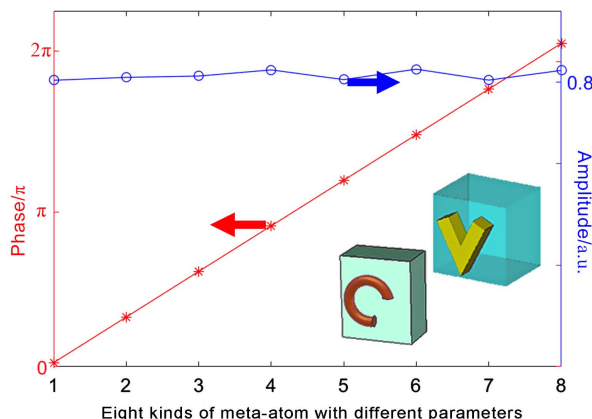
The phase modulation relies on the abrupt phase discontinuity caused by the scattering of subwavelength meta-atoms, such as V-shaped metal [78], C-shaped metal [116], and block metal [106]. A single V-shaped/C-shaped antenna supports two orthogonal electric dipole modes excited by the orthogonal polarizations of light, a symmetric mode and an antisymmetric mode. These two modes offer an extra degree of control of the wavefront scattered from the antenna. As shown in Fig. 12, the phase of the scattered light can be controlled independently of the amplitude by tuning parameters such as the length of the antenna arms and the orientation of V-shaped antennas, and the opening angle and orientation of C-shaped antennas. However, such plasmonic metasurfaces suffer from low efficiency caused by the intrinsically high losses of metals at optical frequencies. Further, these metasurfaces naturally support multiple modes, such as normal reflection/transmission modes and anomalous transmission/reflection modes; among them, only the anomalous reflection/refraction modes are desired [117]. The disadvantage of low efficiency in transmission can be mitigated

Table 2. Various Types of Metasurfaces

Phase Type	Material	Operating Mode and Efficiency	Meta-Atom
Plasmonic resonant phase	Metal	Reflection: 80% [106]; Transmission: ~10% [107]	
Geometric phase/PB phase	Metal/dielectric	<ul style="list-style-type: none"> • Metal type: Reflection: 80% [91]; Transmission: 4.5%–91% [108,109] • Dielectric type: Transmission: 78%–82% [110,111] 	
Huygens' principle based	Dielectric	Transmission Theoretical: ~100% Experimental: ~86% [112]	
Propagation phase/Waveguide phase	High- <i>n</i> dielectric	Transmission Theoretical: ~92% Experimental: ~82% [113]	
Circuit phase	Metal	Reflection: 40% [114] Transmission: 86% [115]	

by metal–insulator–metal (MIM) structures working in a reflection configuration, or a more complicated multilayer design [118].

By precisely controlling the size of the metal block, phase modulation can also be realized by tuning the localized plasmon resonance (LPR) peak, as shown in Fig. 13. At the resonance frequency of a plasmonic meta-atom, the phase of the scattered light undergoes a jump of π . By placing a metallic mirror underneath the plasmonic metal block, the scattered light undergoes double resonance, thus

Figure 12

Phase and amplitude versus V-shaped/C-shaped meta-atoms with different opening and orientation angles.

introducing a complete 2π modulation range with a near flat amplitude profile. In addition, with the use of a MIM structure, a reflection-type metasurface can reach an efficiency higher than 100% [106].

The mechanism of the resonance in plasmonic or high-index dielectric meta-atoms can be analyzed by the Lorentz model. From the coupled model theory [119], the reflection coefficient r and transmission coefficient t are given by

$$r(\omega) = \frac{\gamma}{j(\omega - \omega_0) + \gamma}, \quad t(\omega) = \frac{j(\omega - \omega_0)}{j(\omega - \omega_0) + \gamma}, \quad (22)$$

where ω_0 and γ are the resonance frequency and damping rate of meta-atoms, respectively. For the metasurface in reflection mode, the MIM structure guarantees the intensity of the reflected light during phase modulation. The reflection coefficient r_{MIM} of the MIM structure can be represented as

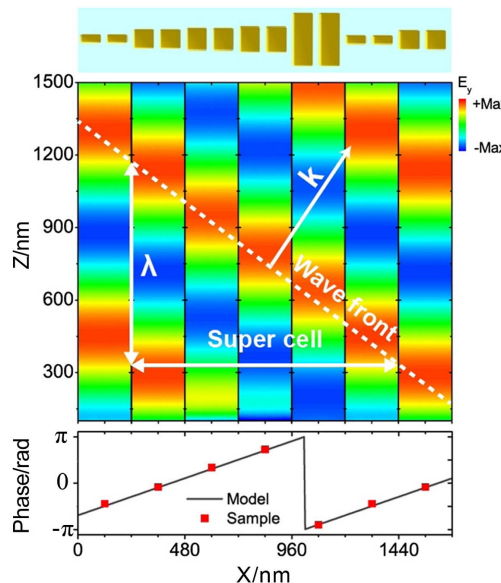
$$r_{\text{MIM}}(\omega) = \frac{j(\omega - \omega_0) - \gamma}{j(\omega - \omega_0) + \gamma}. \quad (23)$$

As shown in Fig. 14, the normalized amplitude of the reflected light (denoted with a red line) is close to unity over a wide range near the resonance frequency peak, while the phase has a phase jump of π .

2.2b. Geometric Phase Type Metasurfaces

The geometric phase, also known as the Pancharatnam–Berry (PB) phase, is derived from the spin rotation effect when circularly polarized light interacts with plasmonic or all-dielectric meta-atoms. The induced geometric phase occurs in crossed polarized light with a value of 2φ , where φ is the in-plane orientation angle of the meta-atom [120]. By controlling the rotation angle of each meta-atom rather than changing the optical path, PB phase modulation is realized, which is more convenient for designing

Figure 13



Resonant metal block array forms a plane wavefront. Reprinted with permission from Sun *et al.*, Nano Lett. **12**, 6223–6229 (2012) [106]. Copyright 2012 American Chemical Society.

a complex phase profile than other optical element design methods. Thus, PB phase modulation is widely applied in a variety of high-performance metasurface holograms.

As is shown in Fig. 15, assuming the meta-atom is mirror symmetric, the local orthogonal coordinate system can be assigned as uv , and the global coordinate system as xoy . The angle between u and x is β . The scattering complex amplitudes along two axes are $t_u = t_1 \exp(i\varphi_1)$ and $t_v = t_2 \exp(i\varphi_2)$. According to the Jones matrix, the scattering property of the meta-atom can be expressed as [121]

$$J = \begin{bmatrix} t_u \cos^2 \beta + t_v \sin^2 \beta & (t_u - t_v)(\sin 2\beta)/2 \\ (t_u - t_v)(\sin 2\beta)/2 & t_u \sin^2 \beta + t_v \cos^2 \beta \end{bmatrix}, \quad (24)$$

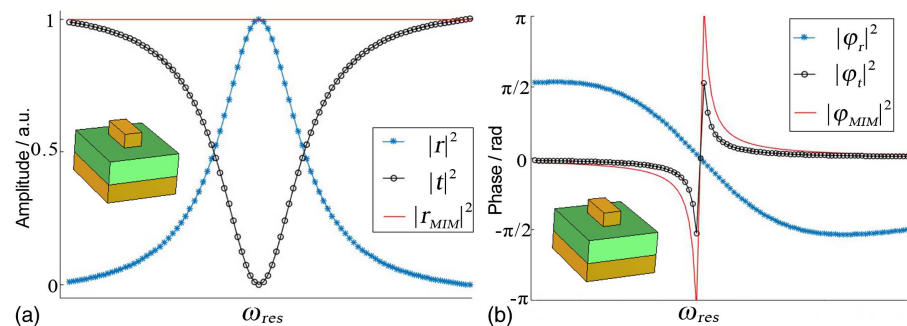
while the electric field of the incident circularly polarized light can be written as

$$\begin{bmatrix} E_{x1} \\ E_{y1} \end{bmatrix} = \frac{E_0}{\sqrt{2}} \begin{bmatrix} 1 \\ j\sigma \end{bmatrix}, \quad (25)$$

where $\sigma = \pm 1$ represent the left- and right-circular polarization of light. Hence, after interacting with the metasurface, the optical field is

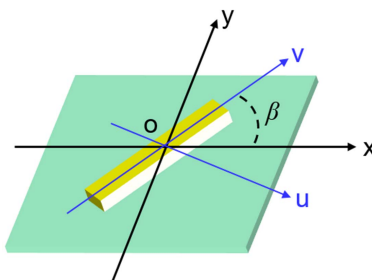
$$\begin{bmatrix} E_{x2} \\ E_{y2} \end{bmatrix} = J \begin{bmatrix} E_{x1} \\ E_{y1} \end{bmatrix} = \frac{E_0}{2\sqrt{2}} \left((t_u + t_v) \begin{bmatrix} 1 \\ j\sigma \end{bmatrix} + (t_u - t_v) e^{j2\sigma\beta} \begin{bmatrix} 1 \\ -j\sigma \end{bmatrix} \right). \quad (26)$$

Figure 14



(a) Amplitude and (b) phase of the reflected light for a single layer meta-atom and the MIM structural meta-atom.

Figure 15



Relationship between coordinate systems for a geometric phase metasurface.

It is clear that the two terms in the above equation represent different polarization states. For the term that has opposite polarization state to the incident wave, it carries an additional phase term of $2\sigma\beta$. The co-polarization term can be omitted if $t_1 = t_2$ and $\varphi_1 - \varphi_2 = 2m\pi + \pi$. To satisfy this condition, the anisotropic meta-atom should act as a half-wave plate.

Metasurfaces based on geometric phase with a simple layer have a low polarization conversion efficiency. There are two methods to overcome this issue. For reflection mode, metasurfaces can be designed as a MIM structure. The meta-atom, dielectric spacer, and metal plate comprise a Fabry–Perot cavity in which light interacts with two metal parts propagating back and forth under the principle of local plasmon resonance, leading to high polarization conversion efficiency. For metasurfaces working in transmission mode, high-index dielectric rods are adopted by designing them to be elliptical posts or rectangular posts. As the propagation phase of the waveguide effect differs by π along the major axis and the minor axis, the dielectric atoms act as a half-wave plate at high transmission efficiency. Compared with other types of metasurfaces, PB phase type metasurfaces have the unique advantage of insensitivity to wavelength, which makes them very useful in designing achromatic optical elements [110,122,123].

2.2c. Huygens' Principle-Based Type Metasurfaces

Huygens' meta-atoms, under the rigorous formulation of the Huygens' principle developed by Love [124], can exhibit very high efficiency in transmission mode. This kind of metasurface was first proposed by Pfeiffer and Grbic in 2013 [115]. The high transmission of Huygens' meta-atoms is the result of simultaneous excitation and mutual interference of magnetic and electric-dipole resonances in high-permittivity all-dielectric nanodisks [125–127]. By interfering electric- and magnetic-induced currents, reflection is canceled.

In Huygens' principle, every point of the wavefront acts as a secondary source of outgoing waves. While the rigorous formulation reveals that in order to achieve purely forward-propagating elementary waves, each individual elementary source should be identified as an electrically small antenna that overlaps electric with magnetic dipole resonances of equal strength [115]. In metasurfaces, under the equivalent surface boundary conditions, the collocated orthogonal electric and magnetic polarizable elements are applied to generate arbitrary field distributions for a given incident field [128].

As shown in Fig. 16, assigning α_e and α_m as the polarizabilities of electric resonance and magnetic resonance for each dielectric meta-atom, together the meta-atoms form a 2D square array, and α_e is orthogonal with α_m . Under the Huygens' principle, the impedance of each dielectric is designed to match that of free space, which can be described as

$$\sqrt{\alpha_m/\alpha_e} = \eta_0, \quad (27)$$

where η_0 is the impedance of free space. Note that the distributions of α_e and α_m with respect to frequencies conform to the Lorentzian line, which can be expressed as

$$\alpha_e = \frac{\alpha_0^e}{\omega_e^2 - \omega^2 - 2j\gamma_e\omega}, \quad \alpha_m = \frac{\alpha_0^m}{\omega_m^2 - \omega^2 - 2j\gamma_m\omega}, \quad (28)$$

where $\omega_{e,m}$, $\gamma_{e,m}$, and $\alpha_0^{e,m}$ are the resonant frequency, damping coefficient, and resonant amplitude, respectively. According to the coupled-mode theory, the transmission coefficient is [104]

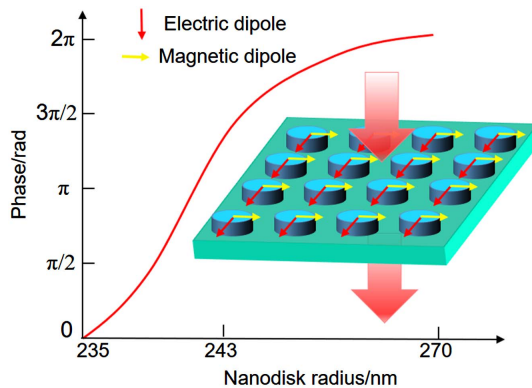
$$t = 1 + \frac{2j\gamma_e\omega}{\omega_e^2 - \omega^2 - 2j\gamma_e\omega} + \frac{2j\gamma_m\omega}{\omega_m^2 - \omega^2 - 2j\gamma_m\omega}. \quad (29)$$

If the electric and magnetic resonances are separated, with $\omega_e \neq \omega_m$, the amplitude and phase spectra are the simple superposition of two individual resonances, as shown in Fig. 17. The amplitudes exhibit resonant dips and the phase range covers only $-\pi/2 \sim \pi/2$ [blue dashed curve in Fig. 17(b)]. In the overlapped case with $\omega_e = \omega_m$, the two resonant modes interfere with each other, the overall transmission efficiency is close to unity for a wide spectral range, and the induced phase change can cover the full 2π range [red solid curve in Fig. 17(b)].

2.2d. Propagation Phase Type Metasurfaces

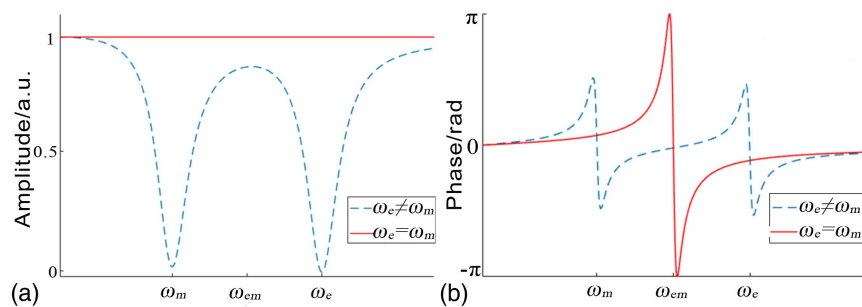
Propagation phase type metasurfaces have a high optical efficiency in transmission mode [113,129,130], and are also referred to as waveguide phase type metasurfaces. Phase modulation originates from the propagation of waveguide modes existing in all-dielectric high-aspect-ratio nanoposts. The effective propagation constant of nanoposts is dependent on size, leading to different phase delay in the transmitted light. As is known, the phase delay of light caused by propagation in the medium can be expressed as $\varphi = k_{\text{eff}} \times d$, where d is the thickness of the medium, and k_{eff} is the

Figure 16



Phase versus radius of the meta-atom based on Huygens' principle. Decker *et al.*, Adv. Opt. Mater. **3**, 813–820 (2015) [128]. Copyright Wiley-VCH Verlag GmbH & Co. KGaA. Adapted with permission.

Figure 17



(a) Amplitude and (b) phase for the separated electric and magnetic dipole resonances and the overlapped electric and magnetic dipole resonances.

effective wave vector of the nanoposts. In the waveguide, k_{eff} can exceed values of naturally occurring optical materials, resulting in a large phase delay without necessitating a very thick medium. Surface plasma waveguide theory and dielectric equivalent refractive index theory are used to design metasurfaces based on propagation phase.

The sandwich structure of metal and insulator is based on surface plasma waveguide theory. The propagation constant of this waveguide varies with the width or thickness of the insulators [131,132]. As shown in Fig. 18(a), the dispersion of the fundamental mode can be represented as

$$\tanh \left(\frac{l \sqrt{k_{\text{sp}}^2 - k_0^2 \epsilon_i}}{2} \right) = \frac{-\epsilon_i \sqrt{k_{\text{sp}}^2 - k_0^2 \epsilon_m}}{\epsilon_m \sqrt{k_{\text{sp}}^2 - k_0^2 \epsilon_i}}, \quad (30)$$

where l is the slit width, k_{sp} is the propagation constant of surface plasma, and ϵ_m and ϵ_i are the permittivity of metal and insulator, respectively. In Eq. (30), k_{sp} can be adjusted by changing the slit width, which could achieve modulation of the local phase.

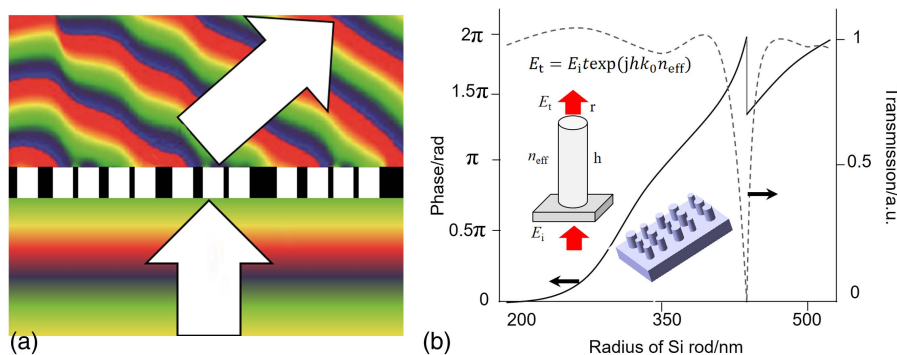
Metasurfaces composed of high-index and low-index dielectric media in a periodic array are based on effective refractive index theory. Phase modulation of the metasurfaces can be realized by changing the size ratio between the different media, namely, the diameter of the dielectric nanoposts in Fig. 18(b) [133]. Dielectric rods of different size modulate the phase from 0 to 2π , while the normalized amplitude can be high as one.

Compared with the Huygens all-dielectric meta-atoms, propagation-phase-based all-dielectric meta-atoms require much higher thickness at the wavelength scale, which increases fabrication challenges. Meanwhile, propagation-phase-based meta-atoms provide more degrees of freedom for full-range phase and polarization control.

2.2e. Circuit Phase Type Metasurfaces

Circuit phase type metasurfaces, composed of metal-layer microstructures, can be modeled by the equivalent circuit model. The equivalent capacitance and inductance are obtained from electromagnetic theory [121]. A single layer transmission type

Figure 18



Metasurfaces based on transmission phase modulation. (a) A deflector consisting of a nanoslit array. (b) The phase and amplitude of a dielectric metasurface as analyzed by waveguide theory. (b) Adapted by permission from Macmillan Publishers Ltd.: Arbabi *et al.*, Nat. Commun. **6**, 7069 (2015) [133]. Copyright 2015.

metasurface is shown in Fig. 19(a). It is assumed that the permittivity and permeability on the two sides of metasurface are $\epsilon_1, \mu_1, \epsilon_2$, and μ_2 , respectively. The reflected and transmitted electric fields in the first medium are A_1 and B_1 , while the transmitted electric field in the second medium is A_2 . In the admittance theory of film structure, the equivalent admittances for free space, metasurface, and media on the sides of the metasurface are Y_0, Y_m, Y_1 , and Y_2 , respectively. The boundary conditions are $A_1 + B_1 = A_2$ and $Y_1 \times (A_1 - B_1) = Y_2 \times A_1 + Y_m \times A_2$. By substituting them into the Fresnel equations, the phases of the reflected wave and transmitted wave can be represented as [121]

$$\varphi_r = \arg\left(\frac{-Y_m/Y_0}{2 + Y_m/Y_0}\right), \quad \varphi_t = \arg\left(\frac{2}{2 + Y_m/Y_0}\right). \quad (31)$$

The two-layer reflection type metasurface, with a metal plate under the metasurface for reflection is shown in Fig. 19(b). The boundary conditions are $A_1 + B_1 = A_2 + B_2$ and $Y_1 \times (A_1 - B_1) = Y_2 \times (A_2 - B_2) + Y_m \times (A_2 + B_2)$, where $Y_2/Y_0 =$. If $Y_1 = Y_0$, the phases of the reflected wave can be [121]

$$\varphi_r = \arg\left(\frac{B_1}{A_1}\right) = \arg\left(\frac{1 - \sqrt{\epsilon_2} - Y_m/Y_0 - (1 + \sqrt{\epsilon_2} - Y_m/Y_0) \exp(2jkd)}{1 + \sqrt{\epsilon_2} + Y_m/Y_0 - (1 - \sqrt{\epsilon_2} + Y_m/Y_0) \exp(2jkd)}\right), \quad (32)$$

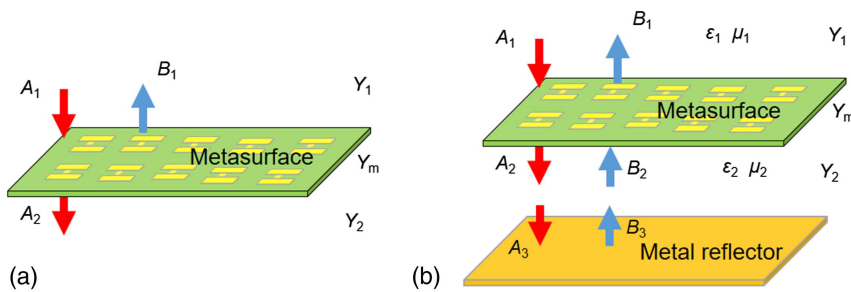
where k is the wavevector of the middle medium and d is the thickness.

Taking I-shaped based metasurfaces as an example [114], as shown in Fig. 20(a), when the width w is changed, the phase shift of the reflected electromagnetic wave will change accordingly. In the case of a normally incident wave with the polarization along the y axis, the I-shaped arm along the x axis serves as the equivalent capacitance C , and the I-shaped arm formed along the y axis acts as the equivalent inductance L . They are connected in series as an LC resonant circuit with a surface impedance of $Z_m = j\omega L + 1/(j\omega C)$. When the incident wave is polarized along the x axis, electromagnetic resonance is not excited, and the metasurface is transparent. The metal film at the bottom ensures a constant reflected amplitude as the phase changes with different parameters of the I-shaped meta-atom. If the absorption of the metal plate is sufficiently small, the reflection efficiency of the surface can approach 100%. Different kinds of meta-atoms based on circuit phase are shown in Fig. 20(b) [114,134,135].

2.2f. Nonlinear Metasurfaces

The nonlinear properties of the material provides a new degree of freedom of frequency to improve the performance of the metasurface [136]. It enables more

Figure 19



Equivalent circuit for (a) transmissive and (b) reflective metasurfaces.

functionality to be integrated into a single optoelectronic circuit as needed. Under the electric dipole approximation, the nonlinear optical response of a material can be described as a power series expansion of the nonlinear material polarization, $\mathbf{P}^{\text{NL}} = \epsilon_0(\chi^{(2)}\mathbf{E}^2 + \chi^{(3)}\mathbf{E}^3 + \dots)$, where ϵ_0 is the vacuum permittivity, \mathbf{E} is the electric field, and $\chi^{(2)}$ and $\chi^{(3)}$ are the second- and third-order nonlinear susceptibilities, respectively. Second and third harmonic generation (SHG and THG) and four wave mixing (FWM) are related to $\chi^{(2)}$ and $\chi^{(3)}$ [137]. Noble metals such as gold, silver, and copper have been shown to have strong second- and third-order nonlinear susceptibilities due to strong electric and magnetic resonances. By combining both organic and inorganic semiconductors with plasmonic meta-atoms to form composite metasurfaces, the nonlinear optical efficiency of such hybrid metasurfaces with SHG efficiency is several orders of magnitude higher than that of naturally occurring materials.

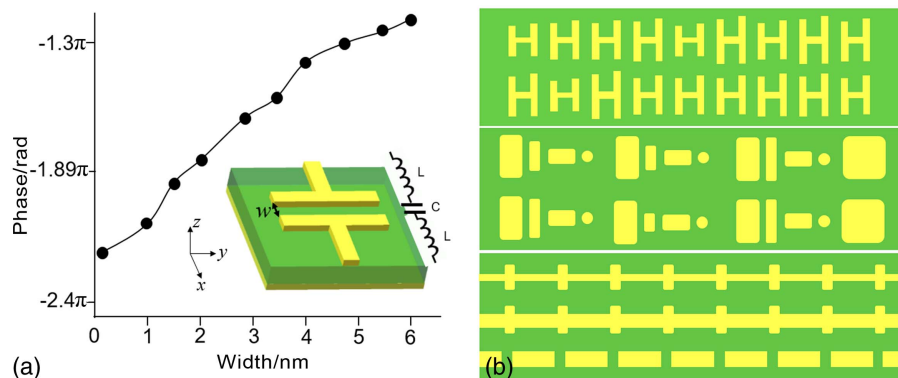
The geometric phase is widely used for phase modulation in nonlinear metasurfaces. For a circularly polarized fundamental wave propagating along the rotational axis of a meta-atom, the locally effective nonlinear dipole moment can be expressed as $\mathbf{P}_\beta^{n\omega} = \alpha_\beta(\mathbf{E}^\sigma)^n$, where α_β is the n th harmonic nonlinear polarizability tensor of the meta-atom with orientation angle β . \mathbf{E}^σ is the electric field of the fundamental wave. The nonlinear polarizability of the meta-atom can be expressed as $\alpha_{\beta,\sigma,\sigma}^{n\omega} \propto \exp((n-1)j\beta\sigma)$ and $\alpha_{\theta,-\sigma,\sigma}^{n\omega} \propto \exp((n+1)j\beta\sigma)$ for harmonic generation with the same or opposite circular polarization compared to that of the fundamental wave [138]. The relative phase factors $(n-1)\beta\sigma$ and $(n+1)\beta\sigma$ of the nonlinear waves depend only on the orientation angle of the meta-atom.

According to the selection rules in harmonic generation for circularly polarized fundamental waves, a single meta-atom with m -fold rotational symmetry allows for only certain harmonic orders [139]. Therefore, by selecting an appropriate local rotational symmetry for the meta-atom, a nonlinear signal consisting of a single spin state with a well-defined nonlinear geometric phase in the range $0 - 2\pi$ can be obtained, as shown in Fig. 21.

3. WHEN METASURFACE MEETS HOLOGRAM

As mentioned above, SLMs, dielectric gratings, and optical antennas can be used to manipulate the wavefront of the computer-generated hologram. However, phase

Figure 20



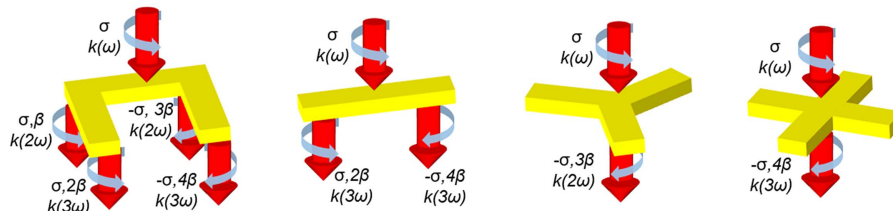
Reflective metasurface devices based on circuit-type phase modulation. (a) Phase response versus the width w for each meta-atom. (b) Different kinds of meta-atoms based on circuit-type phase. Adapted from [114] under the terms of the Creative Commons Attribution 3.0 Unported License. With copyright permission.

manipulation in all these elements relies on light propagation over distances at least 100 times greater than the wavelength. The larger the phase, the greater the phase change of the effective wavefront shaping. In addition, the thicker the element, the more limited the refractive index of the natural material will be. Thus the integration and miniaturization of the optical system are inevitably limited. To achieve a holographic display with a reasonable screen size, the SLM requires an extremely large number of pixels with a small pixel pitch, because the total number of pixels is directly related to the SBP. However, pixel sizes of current SLMs are of the order of micrometers, causing the holograms to suffer from low resolution, low signal-to-noise ratios, small viewing angles, undesired high order diffraction, and twin image issues. Therefore, to maximize the advantages of holographic display, light modulating pixels need to be spaced near to or below the wavelength.

A great deal of research on plasma theory has brought beam steering into the sub-wavelength scale. In recent years, metasurfaces have been used for the reconstruction of holograms with high-quality images. The implementation of a metasurface hologram is shown in Fig. 22. In general, the procedure for designing and displaying metasurface holograms consists of the following steps [140]:

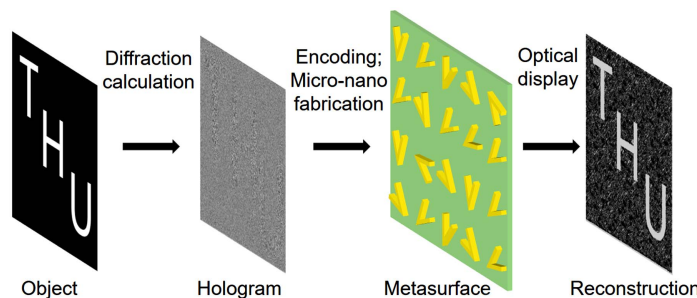
- (i) Formulating the mathematical models of the object and of the hologram.
- (ii) Calculating the complex hologram in the hologram plane.
- (iii) Encoding the phase and/or amplitude on the metasurface, specifically, the information on each pixel of the hologram is loaded onto the metasurface by changing the parameters of each meta-atom.

Figure 21



Nonlinear phase elements with one-, two-, three-, and four-fold rotational symmetry (C1–C4). Based on the rotational symmetry, only particular nonlinear processes and circular polarization states are allowed. Adapted by permission from Macmillan Publishers Ltd.: Li *et al.*, Nat. Rev. Mater. **2**, 17010 (2017) [139]. Copyright 2017.

Figure 22



Implementation of a metasurface hologram.

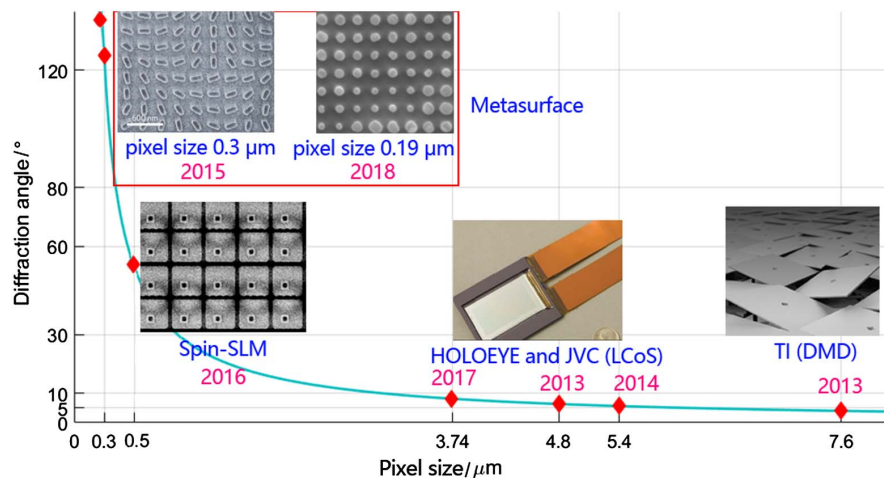
- (iv) Fabricating the metasurfaces through nanofabrication techniques, such as EBL, FIB, nanoimprinting, or atomic layer deposition (ALD).
- (v) Reconstruction of the holographic image by a conventional optical scheme.

With subwavelength meta-atoms, metasurface holograms can even achieve a subwavelength resolution of 350 nm under visible light. In addition, metasurface holograms have an enlarged viewing angle, higher SBP, and suppressed higher order diffraction in the far field. It was quickly recognized that metasurfaces have considerable potential in holography [141]. As is shown in Fig. 23, compared to currently commercially available wavefront modulation devices and other non-metasurface wavefront modulation devices that are not commercially available, metasurfaces perform very well [47,48].

Besides diffraction angle, the diffraction efficiency is also a key parameter for wavefront modulation devices. Metasurface holograms can work in both reflective and transmission modes. Reflective MIM metasurfaces can easily achieve very high working efficiencies, but they suffer from the issue of wave interference, which is inconvenient for realistic applications on some occasions. Therefore, holograms using transmission metasurfaces are also investigated. In Table 3 [142–151], the diffraction efficiencies of metasurface holograms of the recent works are listed.

Metasurface holograms can be classified in many ways. Since the amplitude, phase, and polarization can be modulated simultaneously or independently by each meta-atom, we can classify the metasurface hologram from the perspective of information multiplexing. Specifically, the metasurface holograms are divided into non-multiplexing, polarization multiplexing, wavelength multiplexing, complex amplitude, nonlinear, dynamic, and multiple multiplexing types. In addition to these, there are holograms that use other multiplexing methods, such as spatial multiplexing holography [92], angular multiplexing [152] and others, which are not listed here. Such multiplexing technologies can be used as a platform for low-cost, high-performance, and large capacity holographic displays and data storage systems.

Figure 23



Historical evolution of pixel size and diffraction angle of spatial light modulation technologies.

Table 3. Efficiency of Different Transmission Type Metasurface Holograms

Material	Polarization	Wavelength	Diffraction Efficiency	Fabrication and Meta-Atom	Phase Type and CGH Algorithms	References
c-Si	Independent	532 nm	40%	ICP etching Post: Diameter 82–152 nm, height 270 nm EBL	Waveguide phase; GS algorithm	[142]
poly-Si	Independent	532 nm	6%	Post: Diameter 66–111 nm, height 230 nm EBL	Waveguide phase; Fourier hologram by GS algorithm	[143]
Cr	Independent	532 nm	2%	Hole: radius of 150 nm ALD and EBL	Genetic algorithm Geometric phase;	[144]
TiO ₂	Circular	480–640 nm	80%	Pillar: 250 nm × 85 nm × 600 nm	GS algorithm	[23]
Au	Circular	Colorful; visible	3%	EBL Nanoslit: 250 nm × 100 nm EBL	Geometric phase; GS algorithm; point source algorithm	[111]
Cr	Independent	405–632.8 nm	0.98%	Elliptical nanohole: 280 nm × 150 nm	Geometric phase; GS algorithm	[145]
a-Si	Linear	480–680 nm	3%	EBL Elliptical nanorod: 190 nm × 100 nm × 370 nm	Geometric phase; GS algorithm; Fresnel region	[146]
a-Si	Independent	473–700 nm	31%	ICPECVD and EBL Post: Diameter 110–200 nm, height 350 nm	Huygens' principle; GS algorithm	[147]
Au	Circular	633 nm 780 nm	~1%–6%	EBL Coupled dimers: 350 nm × 75 nm × 40 nm, gap size of 50 nm EB-PVD and FIB	Geometric phase; 3D Fienup algorithm	[148]
Au	Linear	676 nm	10%	V-shaped antenna: thickness 30 nm; width 30 nm PECVD and EBL	Plasmonic resonance phase; point-based algorithm	[93]
a-Si	Linear	915 nm	84%–91%	Post: diameter 65–455 nm, height 715 nm EBL	Waveguide phase; GS algorithm	[113]
a-Si	Linear	1000–1400 nm	75%	Nanofin: 350 nm × 85 nm × 1000 nm LPCVD and EBL	Geometric phase detour phase	[149]
Si	Independent	1477 nm	40%	Nanodisks: height 243 nm, diameter 534 nm EBL	Huygens' principle; GS algorithm and the angular spectrum method	[150]
a-Si	Independent	1600 nm	90%	Nanopillars: height 865 nm, radius 79–212 nm	Huygens' principle; band-limited angular spectrum method and the GS algorithm	[151]

3.1. Metasurface Holograms without Multiplexing

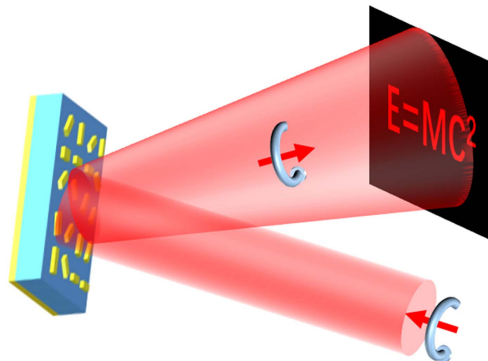
Metasurfaces based on plasmon resonance and PB phase have a wide operating wavelength range since the meta-atoms show the same phase responses for different wavelengths. Such metasurfaces are regarded as the wavelength-insensitive type.

The V-shaped nanoantennas and complementary V-shaped nanoantennas based on Babinet's principle are typically structures in plasmon resonance metasurfaces.

Zheng *et al.* combined the geometric phase control of plasmonic metasurfaces with MIM reflective arrays to yield a high-efficiency reflective metasurface hologram with 16-level phase modulation [91], as is shown in Fig. 24. The phase-only computer-generated hologram was obtained by the GS algorithm, and the Rayleigh–Sommerfeld diffraction method was used to simulate the holographic image because of the large angular range. Similar to the half-wave plate, the reflections along the long axis and the short axis of the nanorod antenna are designed to have a phase difference of π to completely convert a circularly polarized beam into the oppositely polarized one. By blocking transmission with a grounded metal film and improving polarization conversion efficiency, this reflective phase-only metasurface hologram can attain 80% diffraction efficiency at 825 nm and greater than 50% diffraction efficiency over a wide bandwidth of 630–1050 nm, which makes metasurface holograms more practical than conventional holograms.

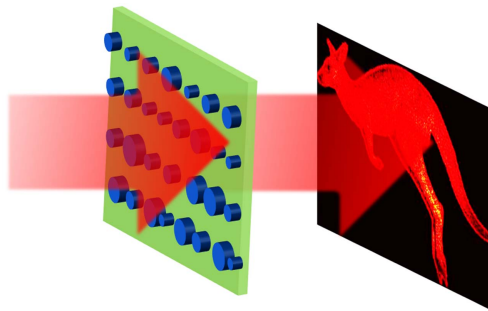
Another approach to realize wavelength-insensitive holography is based on Huygens' principle. A dielectric Huygens' metasurface consisting of silicon nanopillars with 36 different radii, ranging from 79 to 212 nm, has been experimentally demonstrated to transmit over 90% of the incident light with a diffraction efficiency of over 99% at the wavelength of 1600 nm [151]. The hologram, which was designed by the band-limited angular spectrum method and the GS algorithm, is encoded on a $750 \mu\text{m} \times 750 \mu\text{m}$ metasurface. It produces an image of $5 \text{ mm} \times 5 \text{ mm}$ at a distance of 10 mm, as shown

Figure 24



Wavelength-insensitive metasurfaces with MIM structure.

Figure 25



Wavelength-insensitive and polarization-insensitive metasurfaces based on Huygens' principle.

in Fig. 25. Metasurfaces based on the Huygens' principle are also polarization insensitive. Chong *et al.* employed isotropic silicon nanodisks with different lattice periods to achieve a four-level phase modulation metasurface hologram with 82% transmittance efficiency and 40% imaging efficiency in the near-infrared waveband [150]. The hologram was also obtained by the angular spectrum method and the GS algorithm.

In addition to the Huygens' metasurfaces having features of wavelength and polarization insensitivity, dielectric metasurfaces based on dual magnetic resonance and geometric phase also exhibit these two features. Li *et al.* subtly applied Kirchhoff diffraction to generate an image hologram, which was then encoded in a silicon metasurface [153]. Under arbitrary illumination conditions such as natural broad-spectrum light, the reconstructed image appears to float above the sample structure with a reconstructed distance of 100 nm, as shown in Fig. 26.

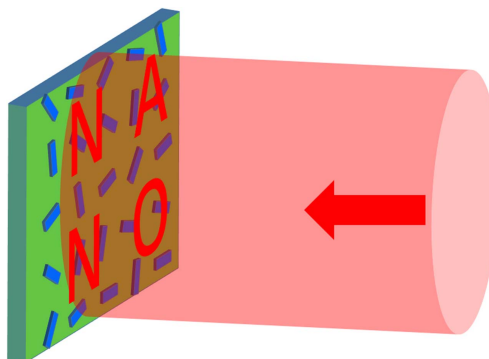
3.2. Polarization-Multiplexed Metasurface Holograms

In traditional optical holography, polarization-dependent holographic multiplexing was applied in natural photo-induced anisotropic materials. In metasurface holography, polarization-multiplexed holography, including linear and circular polarizations, is easy to implement because most metasurfaces can be designed to be anisotropic.

3.2a. Linear-Polarization-Multiplexed Metasurfaces

Anisotropic metasurfaces are sensitive to the incident polarization state. Meta-atoms exhibit different phase responses for different incident polarization states. Different holograms corresponding to the two polarization states can be superimposed and encoded in metasurfaces. Therefore, the reconstructed holographic images can be selected by switching the polarization state of incident light. Chen *et al.* used the MIM reflection type configuration, cross-shaped gold nanorods on top of a dielectric layer based on a gold film, to achieve a four-level phase modulated metasurface hologram for reconstructing dual switchable dual images controlled by the incident linear polarizations [154], as shown in Fig. 27. The IFTA with 100 iterations is utilized for hologram design with rapid convergence. By introducing the gap-plasma mode, the phase of the reflected wave can be tuned independently by changing the length of the nanorod. During reconstruction, the electric dipole resonance of a single nanorod is selectively excited by linear incident light polarized along the nanorod direction. Two distinct images with an experimental efficiency of 18% can be reconstructed under two orthogonal linearly polarized light beams. Using the same principle,

Figure 26

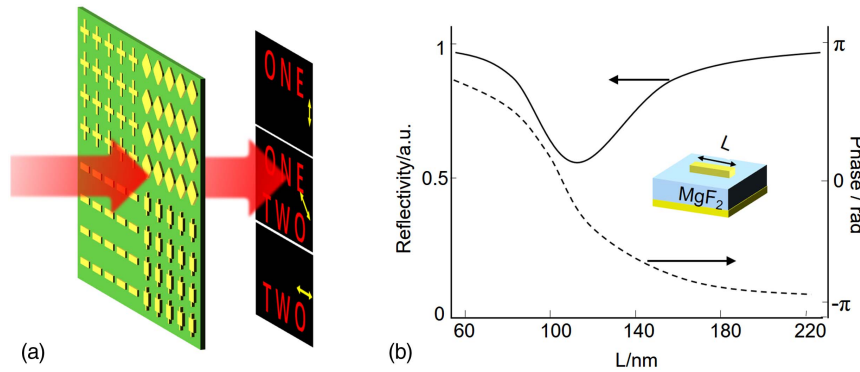


Wavelength-insensitive and polarization-insensitive metasurfaces based on dual magnetic resonances. Adapted with permission from Li *et al.*, ACS Nano **11**, 9382–9389 (2017) [153]. Copyright 2017 American Chemical Society.

Montelongo *et al.* encoded the holographic phase distribution calculated by the GS algorithm in vertically and horizontally oriented silver nanorods with an L shape to achieve a binary-amplitude metasurface [155].

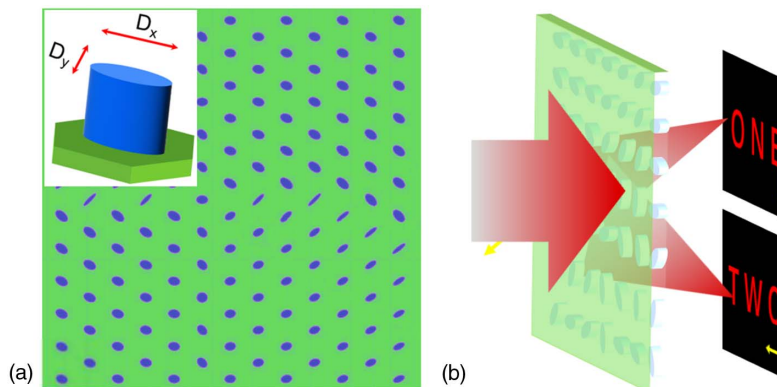
Except for metasurfaces composed of metallic meta-atoms, linear-polarization-multiplexed metasurfaces can also be realized in transmission mode for dielectric materials. Figure 28 shows that the all-dielectric metasurfaces based on propagation phase has realized polarization multiplexing [113]. By using elliptical silicon meta-atoms, each meta-atom can be considered as a waveguide that is truncated on both sides and operates as a low-quality-factor Fabry–Perot resonator. The elliptical cross-section of the waveguide leads to different effective refractive indices of the waveguide modes with the polarizations along the major and minor Axes. As a result, each of the posts imposes a polarization-dependent phase shift on the transmitted light and modifies both its phase and polarization. The major axis and minor axis of the elliptical pillar can be independently tailored to modulate two sets of phase profile.

Figure 27



(a) Linear-polarization-multiplexed metasurface holograms based on cross-shaped gold nanorods. (b) In this meta-atom, the phase and amplitude are controlled by the length of the gold nanorod. (b) Adapted with permission from Chen *et al.*, Nano Lett. **14**, 225–230 (2014) [154]. Copyright 2014 American Chemical Society.

Figure 28



(a) Elliptical silicon posts. (b) Linear-polarization-multiplexed metasurfaces are encoded in two independent phases by the major and minor axes. (a) Adapted by permission from Macmillan Publishers Ltd.: Arbabi *et al.*, Nat. Nanotechnol. **10**, 937–943 (2015) [113]. Copyright 2015.

Thus, two polarization-dependent dual images can be encoded in a single subwavelength unit cell. This design prevents the unwanted high-order diffraction, which results in a high transmission efficiency of over 97%.

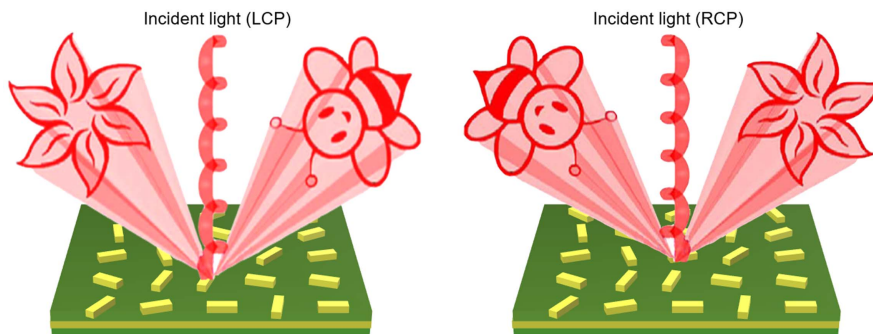
3.2b. Circular-Polarization-Multiplexed Metasurfaces

Circular-polarization-multiplexed metasurfaces are mainly implemented by using the concept of geometric phase. As shown in Fig. 29, two different holograms corresponding to left-circularly polarized (LCP) incident light and right-circularly polarized (RCP) incident light are calculated by the GS algorithm, and then encoded in the MIM structural metasurfaces after superimposition [156]. Identical silver nanorods with different orientation angles can not only provide nearly continuous 16-level phase profiles over the entire 2π range, but also provide uniform reflection amplitude by eliminating the unintended amplitude variations caused by the different size of the nanorods. The holograms exhibit an efficiency of 59.2% at 860 nm and over 40% over 475–1100 nm. Two reconstructed images, a flower and a bee, exhibit helicity dependent behaviors. In the CGH, the phase shift method is used to stagger the reconstructed images.

The circular-polarization-multiplexed metasurface can be further extended by combining the geometric phase and the detour phase [149], or by combining the geometric phase with the propagation phase. For example, when combining the geometric phase and the propagation phase, any orthogonal polarization (including linear, circular, and elliptically polarized) multiplexing schemes can be realized. Balthasar Mueller *et al.* demonstrated a chiral hologram characterized by a fully independent far field for each circular polarization in the visible [157]. The hologram corresponding to two cartoon images in the far field was calculated by using the GSA, as shown in Fig. 30. The metasurface, composed of non-interacting elliptical TiO₂ pillars, is designed to exert these phase profiles independently of each circular polarization in transmission.

In addition to polarization multiplexing of images, orbital angular momentum can also be polarization multiplexed in multiple channels. Chen *et al.*'s work simultaneously realizes a polarization-controllable hologram and superposition of orbital angular momentum. By continuously controlling the polarization state of the incident light, the polarization-dependent holographic images in two channels along the horizontal direction and the continuous control of orbital angular momentum superposition in two channels along the vertical direction are realized [158]. In addition to planar

Figure 29



Circular-polarization-multiplexed metasurface holograms based on PB phase. The holograms corresponding to different helicity of incident circular polarizations are encoded in silver nanorods. Adapted from [156] under the terms of the Creative Commons Attribution 4.0 International License. With copyright permission.

metasurfaces, curved metasurfaces are also designed for circular-polarization-multiplexed metasurface holograms [159,160].

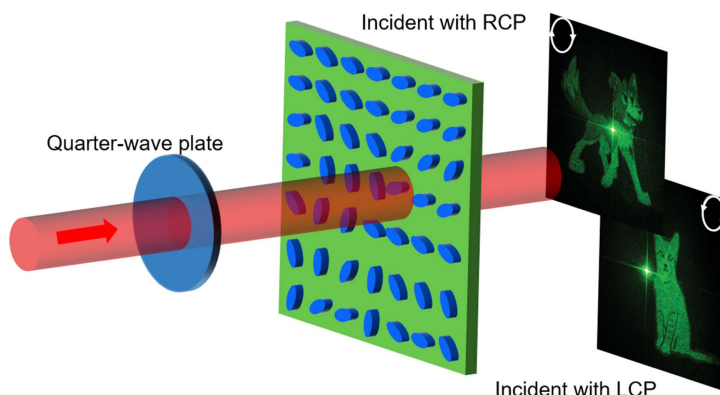
3.3. Wavelength-Multiplexed Metasurface Holograms

With the purpose of expanding information capacity and realizing color holographic display, phase information is encoded at a plurality of wavelengths in wavelength-multiplexed metasurfaces. In conventional holography, colorful images can be obtained by the rainbow hologram. However, such holograms produce only horizontal parallax, and the viewing angle is limited. Colorful holograms can also be constructed by encoding the computer-generated hologram based on the SLM. However, issues such as poor image quality, limited color gamut, and narrow viewing angle are evident. In metasurface holography, there are two ways to implement color holography. One approach is to design different plasmonic resonant meta-atoms with various geometric size and narrow bandwidths, then combine these unit cells into a supercell. Multiple meta-atoms in each supercell can resonate at separate wavelengths. Another method is to encode a variety of holographic information associated with different colors within meta-atoms of uniform geometric size. Three CGH holograms calculated separately for the red, green, and blue components are superposed with additional phase shifts for each color. The reconstructed image can eliminate crosstalk by changing the incident angles of the beams at different wavelengths. During the reconstruction process, incident illumination by three laser beams at different oblique angles is used to decode the three color components to produce the desired full color image.

3.3a. Metasurface Based on Multiple Kinds of Meta-Atoms

In research by Tsai and co-workers, a MIM structure metasurface composed of three pairs of meta-atoms possessing resonance peaks at 405, 532, and 658 nm was used to encode a binary-phase hologram. Each meta-atom modulates the binary phase (0 and π) in accordance with the length of a nanorod. Each supercell is designed to contain four kinds of meta-atoms, each of which corresponds to a reflected color. Due to the low reflection amplitude of red light, one more meta-atom array is used to increase the reflection amplitude of red light [161]. Since both the wavelength multiplexing and phase modulation rely on the resonant feature of the nanorod meta-atoms, only

Figure 30

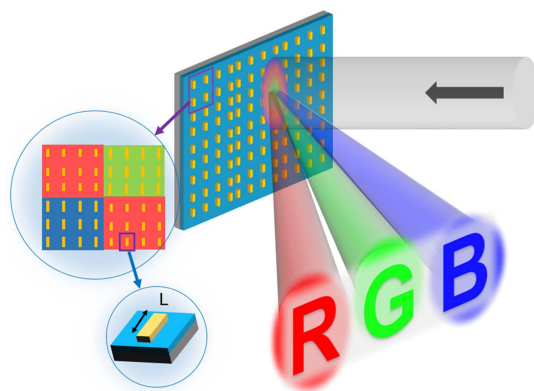


Circular-polarization-multiplexed metasurface holograms based on the combination of PB phase and propagation phase. Elliptical TiO₂ posts are used as meta-atoms. Figure 2(a) adapted with permission from Balthasar Mueller *et al.*, Phys. Rev. Lett. **118**, 113901 (2017) [157]. Copyright 2017 by the American Physical Society. <https://journals.aps.org/prl/abstract/10.1103/PhysRevLett.118.113901>.

two-level phase modulation is applied to the holographic images. As is shown in Fig. 31, images of the letters R, G, and B are reconstructed with corresponding colors. Because of the limited phase levels and the large size of the super unit cell, multiple high-order images appear in the imaging plane.

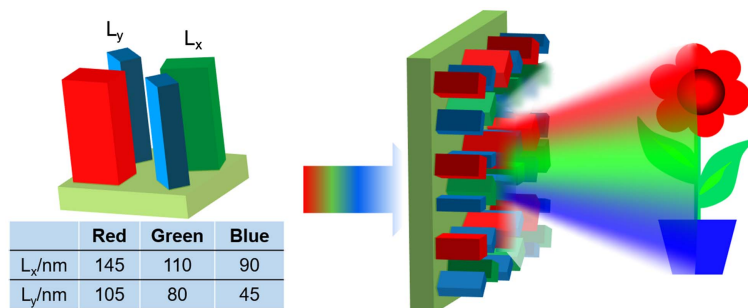
By increasing the phase modulation level, metasurfaces are able to reconstruct complex images with more detail. A computer-generated hologram with eight-level phase modulation is encoded in geometric phase metasurfaces [162]. A metasurface with three kinds of silicon bricks of different sizes has enhanced diffraction peaks at 473, 532, and 633 nm. Under white-light illumination, for each brick, only the wavelength corresponding to the diffraction peak of the brick is emitted, while other wavelengths are localized in the brick. As shown in Fig. 32, a colorful flower was

Figure 31



Wavelength-multiplexed metasurface based on resonant phase. Each super unit cell contains four meta-atoms consisting of an array of aluminum nanorods. Holographic images in the three primary colors, red, green, and blue, are displayed. Adapted with permission from Huang *et al.*, *Nano Lett.* **15**, 3122–3127 (2015) [161]. Copyright 2015 American Chemical Society.

Figure 32



Wavelength-multiplexed metasurfaces based on PB phase. Each super unit cell contains four meta-atoms consisting of silicon bricks. The orientation modulates the phase profile of the hologram, while the size of the meta-atoms determines the resonant frequencies, which present three primary colors. Adapted with permission from Wang *et al.*, *Nano Lett.* **16**, 5235–5240 (2016) [162]. Copyright 2016 American Chemical Society.

successfully constructed. By further increasing the phase modulation level to 16 levels, more complex images can be reconstructed [163].

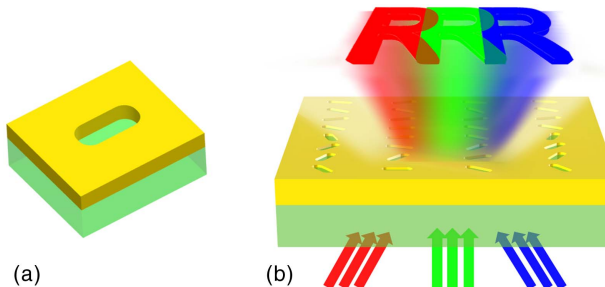
3.3b. Metasurface Based on a Single Kind of Meta-Atom

Super unit cells composed of multiple kinds of meta-atoms do achieve colorful holograms. However, multiple meta-atoms in the super unit cell inevitably increase the pixel size, which reduces the resolution [105]. By using metasurfaces that contain only a single kind of meta-atom, the resolution can be improved and the unwanted high-order images can be avoided. However, each meta-atom needs to function for three colors simultaneously, which may result in color crosstalk. For example, under red-light illumination, the reconstructed image contains not only the red pattern but also the unwanted image patterns designed for green and blue light. The apparent color crosstalk can be seen in the work of Qin *et al.* [164]. In their work, holograms corresponding to three colors are overlapped and then encoded in a nanoslit-type metasurface. One way to overcome this problem is by adding phase shifts to the holograms to stagger images corresponding to different colors. Wan *et al.* reconstructed 2D and 3D full-color images by using an ultrathin single-layer metasurface based on geometric phase [165]. The two-level amplitude and eight-level phase are manipulated by changing the length and rotation angle of the metallic nanoslit. Through the combination of the three primary colors of red, blue, and green, the secondary colors of cyan, magenta, and yellow are also obtained, thereby expanding the color range, as shown in Fig. 33. In addition to the geometric phase, metasurfaces based on the resonance phase are also used to reconstruct colorful images, converting the undesired waves into evanescent ones [111].

3.4. Complex Amplitude Metasurface Hologram

Phase-only SLMs and amplitude-only SLMs are widely used in conventional hologram reconstruction. For a phase-only hologram, the speckle noise is not negligible, while for amplitude-only holograms, the DC noise and twin-image problems are also troublesome. Only the complex hologram can reconstruct the object without losing any information. To improve the image quality of holographic display, complex amplitude modulation has been proposed. Conventional SLMs cannot modulate both the phase and amplitude simultaneously and independently [166]. To break through this limitation, the multi-SLM, the space-division modulation-based single-SLM, and the super pixel methods have been proposed [167]. Figure 34 shows one of these methods.

Figure 33



Wavelength-multiplexed metasurface based on PB phase. Each meta-atom (a) modulates three different primary colors by shifting different incident angles for different light wavelengths, thus forming the colorful image (b). Adapted with permission from Wan *et al.*, ACS Nano **10**, 10671–10680 (2016) [165]. Copyright 2016 American Chemical Society.

Nevertheless, all these methods are at the expense of low resolution, large pixel size, and high response time delay.

Taking advantage of complex amplitude modulation, a metasurface is able to reconstruct images without twin images, and also possesses low speckle noise [93,116,150,168,169]. One of the metasurfaces based on complex amplitude modulation was realized under the principle of PB phase [170]. By rotating the nanorod through an angle of θ , the transmitted cross-polarized light carries an additional phase of 2θ . Hence, if the X-shaped meta-atom shown in Fig. 35(a) is adopted, the complex amplitude of the outgoing light is

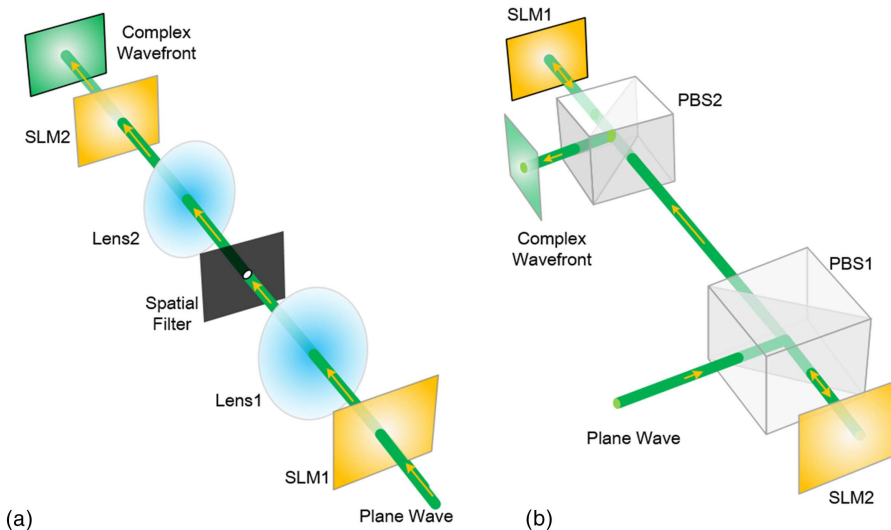
$$E_{-\sigma} \propto 2 \cos(\theta_2 - \theta_1) \exp[j\sigma(\theta_2 + \theta_1)], \quad (33)$$

where θ_1 and θ_2 are the respective rotation angles of the two nanorods comprising the X-shaped meta-atom, and σ represents the polarization state. The term $\cos(\theta_2 - \theta_1)$ modulates the amplitude of the complex amplitude, while $\exp(j\sigma(\theta_2 + \theta_1))$ controls the phase term.

Lee *et al.* proposed complex amplitude modulation by using the aforementioned metasurfaces [170]. Three complex amplitude holograms corresponding to three images of letters at different z positions are calculated by the angular spectrum method and then superimposed into one hologram before being encoded in a metasurface. To demonstrate the advantage of complex amplitude modulation compared to phase-only modulation in such metasurface, a phase-only computer-generated hologram obtained by the angular spectrum method is also encoded in this kind of metasurface. The reconstructed images shown in Fig. 35(b) reveal that complex amplitude modulation of metasurfaces can present improved images with suppressed speckle noise.

However, the metasurface in Lee's work possesses a low efficiency. By combining the geometric phase and dynamic phase, Song *et al.* proposed another metasurface that can generate selective diffraction orders based on a dielectric metasurface with complex amplitude modulation [171]. In their method, the amplitude is manipulated by modulating the geometric parameters in several normalization stages; the desired

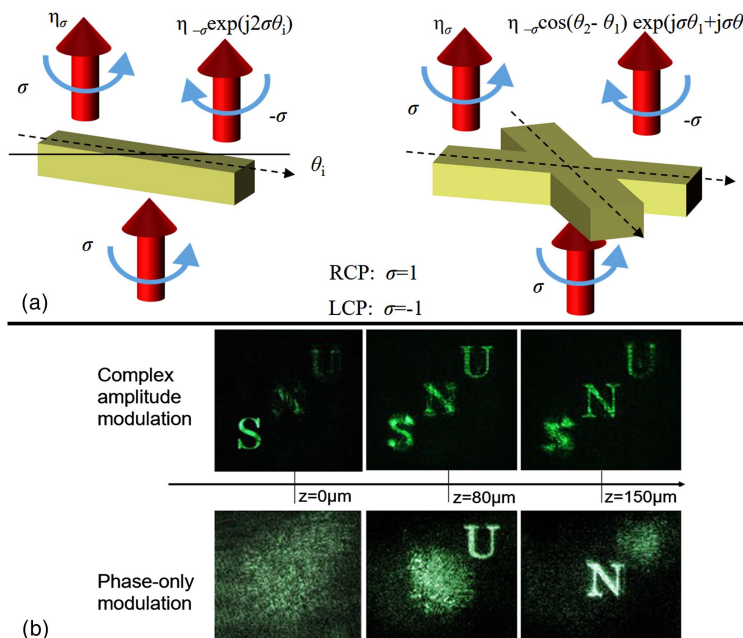
Figure 34



Complex amplitude modulation with two (a) transmissive SLMs and (b) reflective SLMs.

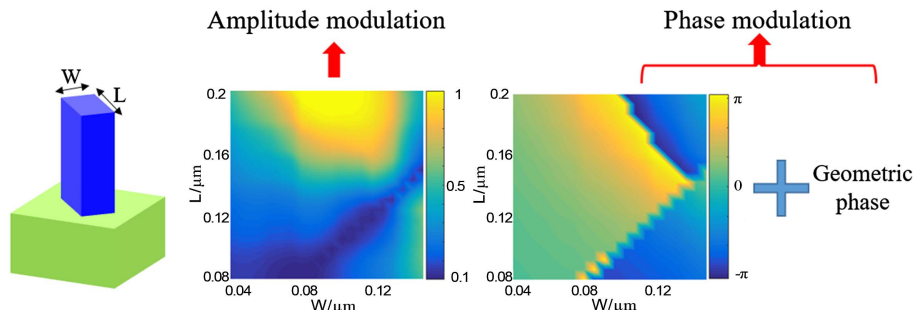
phases are continuously controlled by the orientation angles of nanofins and the dynamic phase, as is shown in Fig. 36. The feature of generating selective diffraction orders in this method has potential for application to beam shaping, parallel laser fabrication, laser cooling, and nanoscale optical detection. Furthermore, a

Figure 35



Complex amplitude metasurface hologram based on PB phase. (a) An X-shaped silicon nanorod acts as a meta-atom. The difference between the two rotation angles modulates the amplitude, while the sum of these two angles modulates the phase. (b) Comparison of the quality of two holographic images obtained by complex amplitude modulation and phase-only modulation [170]. Adapted with permission from Lee *et al.*, *Nanoscale* **10**, 4237–4245 (2018) [170]. Copyright 2018 Royal Society of Chemistry.

Figure 36



Amplitude can be manipulated by modulating the geometric parameters in several normalization stages, the desired phases are continuously controlled by the orientation angles of nanofins and the dynamic phase. Song *et al.*, *Adv. Opt. Mater.* **6**, 1701181 (2018) [171]. Copyright Wiley-VCH Verlag GmbH & Co. KGaA. Adapted with permission.

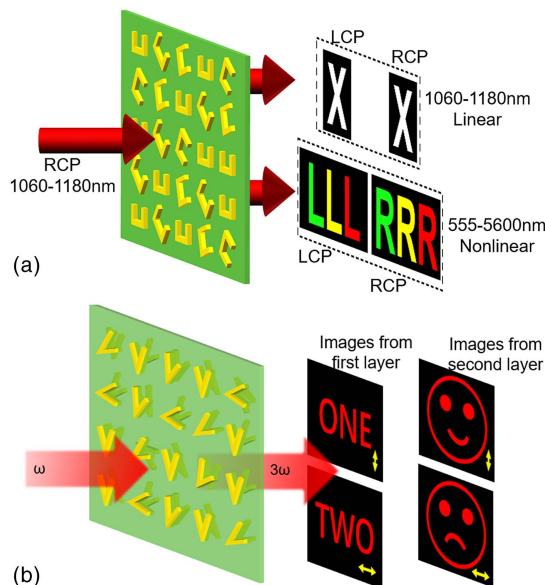
transmissive-type ultrathin metasurface based on multipole resonances is proposed to realize complex amplitude modulation for arbitrary field distributions [172]. The polarization conversion efficiency is higher than 99%, while the thickness is only $\lambda/6$.

3.5. Nonlinear Holographic Metasurfaces

Inspired by linear phase elements, nonlinear metasurfaces have been demonstrated [173,174]. In nonlinear optics, the strong confinement of light to subwavelength regimes that occur naturally in most metasurfaces promotes enhanced nonlinear optical processes. Similar to the response of a linear metasurface, the amplitude, phase, and polarization of the local nonlinear response of the metasurfaces can be tuned by modifying the geometry. Hence, nonlinear multiplexing is achieved by encoding different information in different harmonic wavelengths. Compared to linear metasurface holograms, nonlinear metasurface holograms operating at harmonic frequencies can eliminate the image background noise at the fundamental wavelength. In general, the nonlinear optical process provides more multiplexing channels for building metasurface holograms for reconstructing multiple complex images, which shows great potential for future applications.

Computer-generated holograms of different images are calculated for different orders of harmonic wavelength, as well as different polarization states [175]. Gold split-ring resonators are used to construct nonlinear metasurfaces. In the linear part, the meta-atom shows strong polarization together with the generation of second-order harmonic wave. Phase-only holograms are encoded in the metasurfaces by applying PB phase in the linear and nonlinear parts. With a circularly polarized light σ at the frequency of ω incident on the metasurface, the output light transmitted by the meta-atom with the rotation angle of α can be divided into three beams, reversed polarization light with an additional phase of 2α and a frequency of ω , co-polarized light with an additional

Figure 37



Nonlinear metasurface hologram. (a) Different information is encoded in both the fundamental wavelength and the SHG wavelength. (b) The V-shaped gold antennas convert the incident fundamental wavelength into THG wavelength. (a) Adapted from [175] under the terms of the Creative Commons Attribution 4.0 International License. With copyright permission.

phase of α and a frequency of 2ω , and reversed polarization light with an additional phase of 3α and a frequency of 2ω . As shown in Fig. 37(a), three images of the letters L, R, and X are reconstructed by linear and nonlinear output beams.

Almeida *et al.* have demonstrated another multilayered nonlinear metasurface hologram with THG [176]. The incident linearly polarized beam at the wavelength of 1266 nm is converted into a cross-polarized beam at the wavelength of 422 nm. Linearly polarizable V-shaped gold antennas of various lengths and arm angles are used as meta-atoms with tunable plasmonic resonances to provide variable phase shifts to the incoming beam. For the rotation angle of ϕ , the output third-harmonic beam will carry an additional phase shift of 3ϕ . A two-layer nonlinear metasurface hologram was fabricated with a separate phase hologram embedded in each metasurface layer to yield the desired far-field image for the incident vertical or horizontal linear polarization, as shown in Fig. 37(b). For the first layer, two letters are generated for the vertical and horizontal polarizations, while for the second, images of happy and sad smiley faces are generated.

3.6. Dynamic Holographic Metasurfaces

SLMs, such as the LCoS and DMD, can modulate computer-generated holograms dynamically to reconstruct dynamic images. However, for the metasurface, once it is fabricated, its meta-atoms cannot be changed and the encoded information is immutable. If the issue of dynamic modulation of a metasurface could be overcome, more applications could be realized. The operating wavelength usually dictates the appropriate material and tuning mechanism to realize dynamic modulation [177]. Many materials, such as phase-transition materials (e.g., $\text{Ge}_2\text{Sb}_2\text{Te}_5$ and VO_2) [178–185], 2D materials (e.g., graphene and borophene) [186–190], tunable printed circuits [191,192], and liquid metal [193,194], have been used to design dynamic metasurfaces. Modulation methods based on these materials depend on different mechanisms. In the mid-infrared wavelength range, carrier density modulation via gating of graphene [195], GaAs [196] or indium tin oxide (ITO) [197] has been employed to modulate metasurface reflectance. Also, thermo-optic tuning of PbTe antennas has yielded actively tunable structures in this wavelength range [198]. In the near-infrared and visible wavelength range, researchers have employed a number of different physical mechanisms to realize active metasurfaces. For example, metasurfaces with integrated liquid crystal active layers have enabled control of light transmittance by applying a direct current bias or heating the liquid crystal [199,200]. The reflectance and transmittance of a metasurface can also be mechanically modulated using electrostatic and magnetic forces [201,202]. Further, carrier density modulation can be applied to control the transmission of all-dielectric Huygens metasurfaces at telecom wavelengths [203]. In the visible region, a plasmonic metasurface with an electrically tunable optical response that operates at strikingly low modulation voltages was also experimentally demonstrated [204]. Table 4 lists various types of dynamic metasurfaces based on the materials and mechanisms mentioned above [167,178,179,183,185–188,191–193,196–199,203–212].

Phase-transition materials can be used to realize real-time reconfigurability of optical field modulation devices. By exploiting the hysteretic metal–insulator phase transition (MIT) of polycrystalline VO_2 films, a lithography-free and rewritable metacanvas is presented [205]. VO_2 undergoes a temperature-driven, reversible transition from the insulating (I) to the metallic (M) phase when heated above its transition temperature ($T_c = 68^\circ\text{C}$). As shown in Fig. 38(a), when heating the VO_2 from room temperature (point A) to T_c (point B), the entire film is still in the I-phase. After reaching temperature T_c , a focused laser spot on the film moves following the path of the pattern of a bear to locally heat the VO_2 to the M-phase (point C). Hence, a nonvolatile M-phase

Table 4. Various Types of Dynamic Metasurfaces

Modulation Methods	Materials and Features	Typical Structures
Thermo-optic effect	<ul style="list-style-type: none"> PbTe: mid IR [198] Ge₂Sb₂Te₅: 1.55 μm and mid IR [178,179] VO₂: far IR [205] and THz [185] Liquid crystal: near IR, of the order of seconds [199]^a 	
Light bump	<ul style="list-style-type: none"> Graphene oxide polymers: visible [206] VO₂: THz; the rate is expected to be 100 fs [207]^b Doped silicon: THz [208] Silicon (PIN) photodiodes: microwave [209] 	
On-load voltage	<ul style="list-style-type: none"> Graphene: THz [186] Printing circuit: microwave [191,192]^c ITO: visible; the rate is 100–700 Hz [204] 	
Mechanical strain	<ul style="list-style-type: none"> PDMS: visible [210] 	
Carrier injection	<ul style="list-style-type: none"> ITO: near IR [197,203,211]^d Graphene: THz [188] GaAs: mid IR [196] VO₂: THz, ~millisecond range [183] 	
Microfluid	<ul style="list-style-type: none"> Liquid-metal-Galinstan: microwave [193]^e Liquid with different index: visible; the rate is at the order of milliseconds [167] 	
MEMS based	<ul style="list-style-type: none"> MEMS-tunable dielectric metasurface [212]^f 	

^aImage adapted with permission from Sautter *et al.*, ACS Nano **9**, 4308–4315 (2015) [199]. Copyright 2018 American Chemical Society.

^bImage adapted with permission from Zhao *et al.*, ACS Photon. **5**, 3040–3050 (2018) [207]. Copyright 2018 American Chemical Society.

^cImage adapted from [191] under the terms of the Creative Commons Attribution 4.0 International License. With copyright permission.

^dImage adapted with permission from Kafaie Shirmanesh *et al.*, Nano Lett. **18**, 2957–2963 (2018) [197]. Copyright 2018 American Chemical Society.

^eWu *et al.*, Adv. Opt. Mater. **5**, 1600938 (2017) [193]. Copyright Wiley-VCH Verlag GmbH & Co. KGaA. Image adapted with permission.

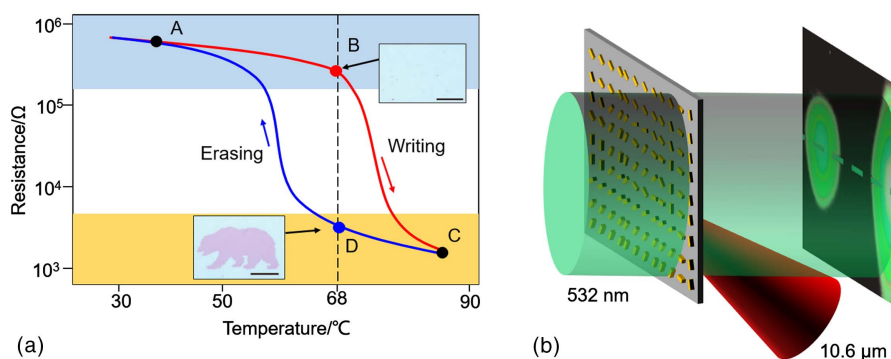
^fImage adapted from [212] under the terms of the Creative Commons Attribution 4.0 International License. With copyright permission.

pattern is written onto the I-phase film. The pattern can easily be erased by reducing the global temperature of the film beyond the I-phase extrema of the hysteresis loop (e.g., to point A). Upon reheating to point B, the film is reset and ready for rewriting a new pattern in the same region. The CGH of an image consisting of two spots was compiled onto the metacanvas. To separate the holographic image from the transmitted main peak without degrading the signal-to-noise ratio, an extra 18 deg

of beam steering phase was added to the hologram. The results are shown in Fig. 38(b).

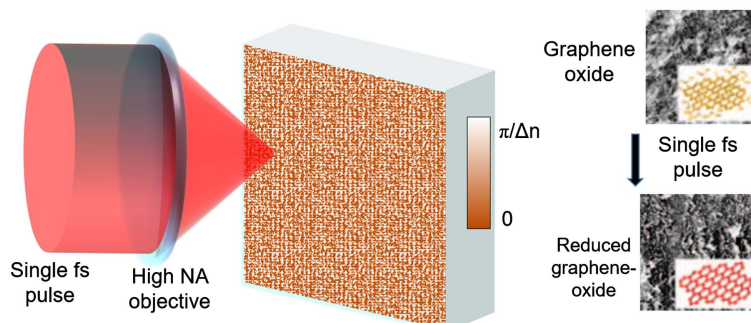
By photoreduction, graphene oxide polymers can be switched between oxidized and reduced states under the control of external temperature, resulting in a change of refractive index. Illuminated by an ultrasmall focused laser spot, graphene in each small region will convert from the oxidized state to reduced state. The encoded information in each region can be changed, as shown in Fig. 39. The 3D images reconstructed by using this dynamic modulation metasurface achieved a view field of 52 deg, which is almost 1 order of magnitude greater than that of the previous method [206]. Such metasurface can also support polarization multiplexing and wavelength multiplexing. All these features make this dynamic modulation metasurface very promising in high-resolution dynamic holographic display if a cheaper femtosecond laser could be realized.

Figure 38



Lithography-free and rewritable metacanvas employing the hysteretic metal–insulator phase transition of a polycrystalline VO₂ film. (a) The resistance of a VO₂ film is temperature dependent [81]. (b) Image of two separated points is reconstructed; the phase pattern is written onto the metacanvas by a focused mid-infrared laser beam. Dong *et al.*, Adv. Mater. **30**, 1703878 (2017) [205]. Copyright Wiley-VCH Verlag GmbH & Co. KGaA. Reproduced with permission.

Figure 39

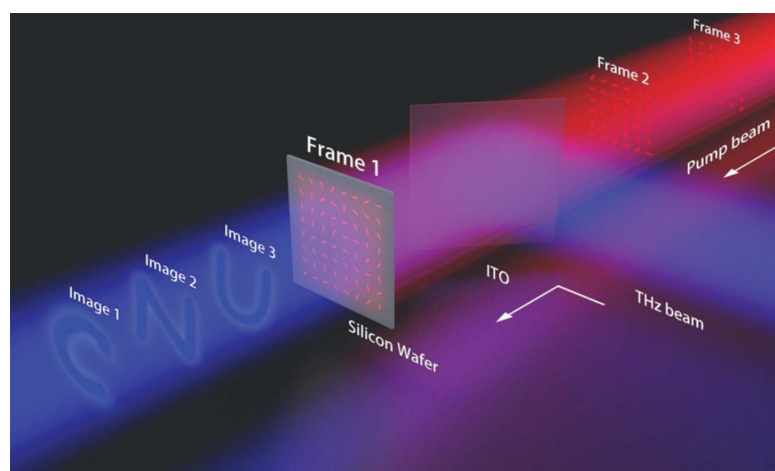


Using photoreduction, the oxidized and reduced states of the graphene oxide polymer are utilized to implement a dynamic metasurface. The transformation is controlled by the external temperature by means of a focused pulsed laser spot. Reproduced from [206] under the terms of the Creative Commons Attribution 4.0 International License. With copyright permission.

Light-controlled current distribution has been used to realize all-optical dynamic metasurfaces in the terahertz regime. Guo *et al.* realized a PB-phase-based dielectric metasurface not by physically fabricating one, but by pumping a thin silicon wafer with structured femtosecond light [208]. The pattern carried by the wavefront of the pump light is translated into a current density distribution on the doped silicon wafer. When the terahertz wave travels through the silicon wafer, the patterned current density distribution acts as a PB phase modulation metasurface. Images of the letters C, N, and U, are refreshed quickly on the reconstruction plane with the change of patterns carried by femtosecond light, as shown in Fig. 40. In this reconfigurable dynamic metasurface, the modulation speed is mainly determined by the response time of the current redistribution, which is less than tens of milliseconds.

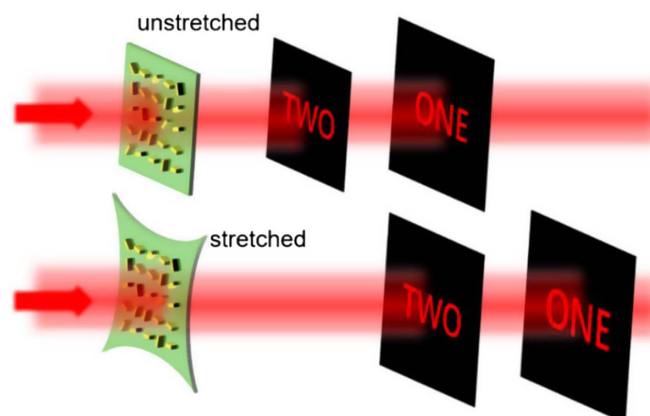
If a metasurface structure is fabricated on a flexible substrate, its period can be changed under stress. This property can be used to design a flat lens with a tunable

Figure 40



Reconfigurable dynamic metasurface in the terahertz regime. Guo *et al.*, *Adv. Opt. Mater.* 7, 1801696 (2019) [208]. Copyright Wiley-VCH Verlag GmbH & Co. KGaA. Reproduced with permission.

Figure 41



Holographic images can be switched to two different patterns with the use of flexible substrate.

focal length. By placing the spatially multiplexed metasurfaces on a flexible substrate, different holographic images can be selected by stretching the substrate or allowing it to relax. As shown in Fig. 41, the reconstruction distance increases as the substrate stretches. Thereby the reconstructed image can be converted from “ONE” to “TWO” on the reconstruction plane [210].

3.7. Multiple Multiplexing Holographic Metasurfaces

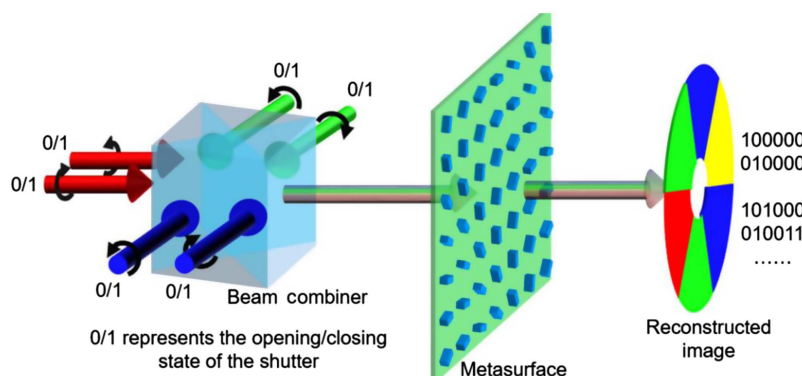
The holographic metasurfaces discussed above possess different kinds of multiplexing channels. To increase the capabilities, extra degrees of multiplexing freedom, such as spatial mode multiplexing [213], orbital angular momentum multiplexing [214] and nonlinear optical multiplexing [175], were exploited. However, the capabilities of these metasurfaces are still limited since each of them possesses only one kind of multiplexing channel. To maximize the information capacity, a multiple multiplexing holographic metasurface, with both polarization-multiplexing and wavelength-multiplexing, is proposed [215,216]. These works realized a 6 bit holographic metasurface with $(2^6 - 1)$ bits of information encoded in color holograms. In research by Qiu and co-workers, the key idea is to obtain the phase profile that operates with the opposite polarizations of three different monochromatic beams [215]. This is solved by using an improved multiwavelength Gerchberg–Saxton (MWGS) algorithm. Two phase profiles, φ_{RCP} controlling red RCP (\hat{R}_{RCP}), green RCP (\hat{G}_{RCP}), and blue RCP (\hat{B}_{RCP}), and φ_{LCP} controlling red LCP (\hat{R}_{LCP}), green LCP (\hat{G}_{LCP}), and blue LCP (\hat{B}_{LCP}), were combined and encoded into a single Si-nanobrick metasurface according to PB phase. Under 6 bit normal incidence, which was achieved by controlling the polarization and on–off state of three monochromatic beams, the reconstructed images were displayed in a combination of different color patterns, as shown in Fig. 42.

This massive number of possible reconstructed holograms arises from the superposition of and permutations of six fundamental independent images. This not only overcomes the crosstalk limitation of single size elements for on-axis illumination, but also realizes a high-capability metasurface with high image quality.

4. CONCLUSIONS AND PERSPECTIVE

A key step in holography is the recording of the wavefront. The advent of CGH makes it possible to reconstruct all kinds of arbitrary 2D/3D objects with arbitrary wavefronts, thus vastly expanding the development of holographic technology. The

Figure 42



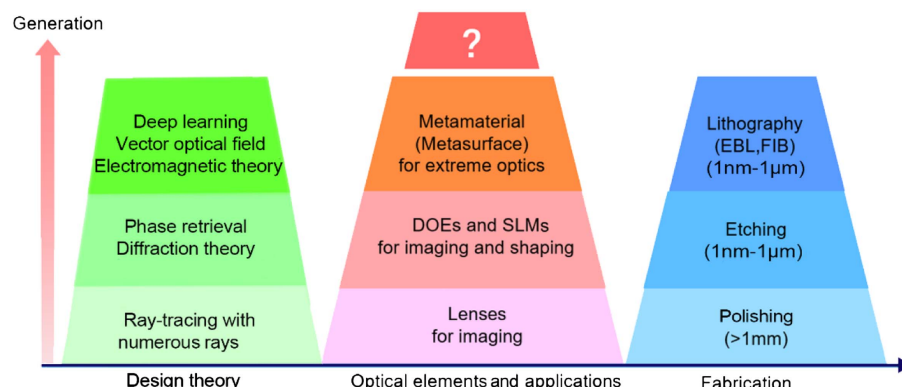
Non-interleaved metasurface for $(2^6 - 1)$ spin- and wavelength-encoded holograms. Adapted with permission from Jin *et al.*, Nano Lett. **18**, 8016–8024 (2018) [215]. Copyright 2018 American Chemical Society.

development of recording media, from photographic films to DOEs, and then to SLMs, prompts the realization of real-time holographic display. Current high-speed 2D and 3D dynamic holographic displays, which encode computer-generated holograms in SLMs, are still stuck with problems such as low resolution, limited viewing angle, and noise. The metasurface hologram, which encodes CGHs in metasurfaces that have a pixel size at the subwavelength scale, provide much higher resolution (~ 300 nm), larger field of view (~ 60 deg), and lower noise than current holograms using the LCoS or DMD SLMs.

Although much progress has been made in the field of metasurface holography, there still exist challenges to be overcome [217]. From diffraction calculation to reconstruction, as shown in Fig. 22, the challenges are listed as follows.

- Information multiplexing. Metasurface holography multiplexing increases the information capacity and makes full use of the SBP. It serves as a platform for large capacity optical data storage, spatial-temporal filtering, information processing, and so on, owing to its unique advantages of parallel recording and multiple multiplexing methods. Current algorithms (point based, polygonal based, GS algorithm, GA, etc.) have already provided many multiplexing methods. Nevertheless, to exploit the powerful capabilities of a metasurface to manipulate the phase, amplitude, and polarization, other accurate, high-precision, and fast scalar/vector theoretical algorithms that can be used for orbital angular momentum multiplexing and multiple nonlinear optical effects are highly in demand.
- The fabrication of metasurfaces. The process of optical metasurface fabrication relies mainly on mature semiconductor manufacturing processes. Among the present semiconductor manufacturing processes, particle beam fabrication methods such as EBL and FIB are high cost and time consuming, while laser fabrication is limited to periodic patterns, and nanoimprint lithography is limited by the manufacturing materials. Therefore, with the rapid development of photonics, fabrication techniques possessing low cost, high speed, high precision, and compatible with large area devices are of interest. A promising avenue is to explore bottom up techniques to assemble plasmonic nanostructures, as well as fabrication on flexible substrates for integration with other devices.
- Real-time reconfigurable metasurfaces. Metasurface holograms are considered to be the most promising technology in the display field, for applications such as cell phones, laptops, and wearable displays for augmented reality [84,218]. To offer a

Figure 43



Development of fabrication, optical elements, and computing theory in each generation.

comfortable viewing experience, the display covering the visible region should have a refresh rate higher than 75 Hz. However, the refresh rate of the full canvas of current reconfigurable metasurfaces in the visible region remains in the several hertz. To realize dynamic 2D or 3D holographic display, it is imperative to explore new modulation mechanisms and novel structures.

Metasurface holograms show great potential for applications in many areas. In information processing, metasurface holograms can be used as spatial filters, beam-shaping elements, deflectors, beam splitters, and optical interconnects, and can also be used for free-space communications and high-performance computing [140]. In computational imaging [219], the metasurface hologram switches the ghost imaging target with different polarizations of light, paving the way to applications in the fields of optical communications, imaging technology, and security. In 3D display, metasurface holograms with high performance, that are dynamically reprogrammable, and provide multiple-channel encoding will open a door to the next generation naked-eye 3D displays. In encryption, metasurface holograms are ideal candidates for encrypted patterns because of the convenient and robust processing of data handling and encryption, due to their high precision and usage of multiple control parameters, which can increase the security level [140,215,216,220]. In addition to these areas, metasurface holograms also have potential applications in areas such as optical metrology [221], optical sensors [222,223], holographic storage [152], and pattern recognition [215,224].

Looking back at the development of optical components, it can be seen that the advancement of manufacturing processes and breakthroughs in optical theory have greatly prompted the development of optical components. Figure 43 gives an intuitive overview of this development. In the early stage, the main manufacturing technology used for optical elements is polishing. Its corresponding minimum linewidth is of the order of millimeters. First-generation optical elements such as prisms and lenses fabricated by polishing are widely used for optical imaging based on ray-tracing theory. With the decrease of minimum linewidth micrometers, second-generation optical components, such as DOEs and SLMs, quickly spread to industrial fields and consumer applications. Based on phase retrieval and diffraction theory, imaging, and beam-shaping devices become lighter. Current manufacturing processes are further enhanced, and the minimum linewidth has decreased to the nanometer scale. At this stage, metamaterials consisting of subwavelength meta-atoms are realized, especially in the visible region. Vector optical fields can be manipulated by metamaterials. Electromagnetic theory is used to design the functional elements. In addition, with the development of the neural network algorithm, the design of metamaterials (like metasurfaces) can even be achieved by deep learning [225–228]. It is foreseeable that with the developments of manufacturing technology, computing performance, and further exploration of dynamic modulation mechanisms, metasurfaces, one of the metamaterials and a next-generation optical component, will bring a revolution in products.

FUNDING

National Natural Science Foundation of China (NSFC) (61775117); National Postdoctoral Program for Innovative Talents of China (BX201700313); China Postdoctoral Science Foundation (2018M630148).

ACKNOWLEDGMENT

The authors would like to thank the editor and the anonymous reviewers for their detailed review and constructive suggestions that contribute much to the

improvements of this paper. The authors sincerely thank Prof. Yan Zhang and Prof. Guixin Li for the valuable comments.

REFERENCES

1. D. Gabor, "A new microscopic principle," *Nature* **161**, 777–778 (1948).
2. E. N. Leith and J. Upatnieks, "Wavefront reconstruction with diffused illumination and three-dimensional objects," *J. Opt. Soc. Am.* **54**, 1295–1301 (1964).
3. Y. N. Denisyuk, "On the reflection of optical properties of an object in a wave field of light scattered by it," *Dokl. Akad. Nauk SSSR* **144**, 1275–1278 (1962).
4. A. W. Lohmann and D. P. Paris, "Binary Fraunhofer holograms, generated by computer," *Appl. Opt.* **6**, 1739–1748 (1967).
5. A. Kozma and D. L. Kelly, "Spatial filtering for detection of signals submerged in noise," *Appl. Opt.* **4**, 387–392 (1965).
6. B. R. Brown and A. W. Lohmann, "Complex spatial filtering with binary masks," *Appl. Opt.* **5**, 967–969 (1966).
7. L. B. Lesem, P. M. Hirsch, and J. A. Jordan, "The kinoform: a new wavefront reconstruction device," *IBM J. Res. Dev.* **13**, 150–155 (1969).
8. S. Fukushima, T. Kurokawa, and M. Ohno, "Real-time hologram construction and reconstruction using a high-resolution spatial light modulator," *Appl. Phys. Lett.* **58**, 787–789 (1991).
9. T. M. Kreis, P. Aswendt, and R. Hoefling, "Hologram reconstruction using a digital micromirror device," *Opt. Eng.* **40**, 926–933 (2001).
10. T. Nishitsuji, T. Shimobaba, T. Kakue, and T. Ito, "Fast calculation of computer-generated hologram using run-length encoding based recurrence relation," *Opt. Express* **23**, 9852–9857 (2015).
11. L. Ahrenberg, P. Benzie, M. Magnor, and J. Watson, "Computer generated holograms from three dimensional meshes using an analytic light transport model," *Appl. Opt.* **47**, 1567–1574 (2008).
12. K. Matsushima and S. Nakahara, "Extremely high-definition full-parallax computer-generated hologram created by the polygon-based method," *Appl. Opt.* **48**, H54–H63 (2009).
13. L. Ahrenberg, P. Benzie, M. Magnor, and J. Watson, "Computer generated holography using parallel commodity graphics hardware," *Opt. Express* **14**, 7636–7641 (2006).
14. T. Shimobaba and T. Ito, "An efficient computational method suitable for hardware of computer-generated hologram with phase computation by addition," *Comput. Phys. Commun.* **138**, 44–52 (2001).
15. A. W. Lohmann, *The Space-Bandwidth Product, Applied to Spatial Filtering and to Holography* (IBM, 1967).
16. T. Kozacki, M. Kujawińska, G. Finke, B. Hennelly, and N. Pandey, "Extended viewing angle holographic display system with tilted SLMs in a circular configuration," *Appl. Opt.* **51**, 1771–1780 (2012).
17. H. Sasaki, K. Yamamoto, K. Wakunami, Y. Ichihashi, R. Oi, and T. Senoh, "Large size three-dimensional video by electronic holography using multiple spatial light modulators," *Sci. Rep.* **4**, 6177 (2014).
18. T. Inoue and Y. Takaki, "Table screen 360-degree holographic display using circular viewing-zone scanning," *Opt. Express* **23**, 6533–6542 (2015).
19. G. Li, J. Jeong, D. Lee, J. Yeom, C. Jang, S. Lee, and B. Lee, "Space bandwidth product enhancement of holographic display using high-order diffraction guided by holographic optical element," *Opt. Express* **23**, 33170–33183 (2015).
20. T. Kurihara and Y. Takaki, "Shading of a computer-generated hologram by zone plate modulation," *Opt. Express* **20**, 3529–3540 (2012).

21. K. Wakunami and M. Yamaguchi, "Calculation for computer generated hologram using ray-sampling plane," *Opt. Express* **19**, 9086–9101 (2011).
22. T. Ichikawa, T. Yoneyama, and Y. Sakamoto, "CGH calculation with the ray tracing method for the Fourier transform optical system," *Opt. Express* **21**, 32019–32031 (2013).
23. J.-S. Chen, D. Chu, and Q. Y. Smithwick, "Rapid hologram generation utilizing layer-based approach and graphic rendering for realistic three-dimensional image reconstruction by angular tiling," *J. Electron. Imag.* **23**, 023016 (2014).
24. J. P. Waters, "Holographic image synthesis utilizing theoretical methods," *Appl. Phys. Lett.* **9**, 405–407 (1966).
25. W. H. Lee, "Sampled Fourier transform hologram generated by computer," *Appl. Opt.* **9**, 639–643 (1970).
26. D. Leseberg and C. Frère, "Computer-generated holograms of 3-D objects composed of tilted planar segments," *Appl. Opt.* **27**, 3020–3024 (1988).
27. J. S. Kollin, S. A. Benton, and M. L. Jepsen, "Real-time display of 3-D computed holograms by scanning the image of an acousto-optic modulator," *Proc. SPIE* **1136**, 178–185 (1989).
28. M. E. Lucente, "Interactive computation of holograms using a look-up table," *J. Electron. Imag.* **2**, 28–34 (1993).
29. M. Yamaguchi, H. Hoshino, T. Honda, and N. Ohyama, "Phase-added stereogram: calculation of hologram using computer graphics technique," *Proc. SPIE* **1914**, 25–31 (1993).
30. H. Yoshikawa and H. Kameyama, "Integral holography," *Proc. SPIE* **2406**, 226–234 (1995).
31. K. Matsushima, H. Schimmel, and F. Wyrowski, "Fast calculation method for optical diffraction on tilted planes by use of the angular spectrum of plane waves," *J. Opt. Soc. Am. A* **20**, 1755–1762 (2003).
32. H. Zhang, N. Collings, J. Chen, B. A. Crossland, D. Chu, and J. Xie, "Full parallax three-dimensional display with occlusion effect using computer generated hologram," *Opt. Eng.* **50**, 074003 (2011).
33. H. Kang, E. Stoykova, and H. Yoshikawa, "Fast phase-added stereogram algorithm for generation of photorealistic 3D content," *Appl. Opt.* **55**, A135–A143 (2016).
34. H. Zhang, Y. Zhao, L. Cao, and G. Jin, "Fully computed holographic stereogram based algorithm for computer-generated holograms with accurate depth cues," *Opt. Express* **23**, 3901–3913 (2015).
35. H. Zhang, Y. Zhao, L. Cao, and G. Jin, "Layered holographic stereogram based on inverse Fresnel diffraction," *Appl. Opt.* **55**, A154–A159 (2016).
36. Z. Huang, D. L. Marks, and D. R. Smith, "Out-of-plane computer-generated multicolor waveguide holography," *Optica* **6**, 119–124 (2019).
37. J. Geng, "Three-dimensional display technologies," *Adv. Opt. Photon.* **5**, 456–535 (2013).
38. T. Seymour, "Computer-simulated Fresnel holography," *Eur. J. Phys.* **21**, 317–331 (2000).
39. Y. Zhao, L. Cao, H. Zhang, D. Kong, and G. Jin, "Accurate calculation of computer-generated holograms using angular-spectrum layer-oriented method," *Opt. Express* **23**, 25440–25449 (2015).
40. N. T. Shaked and J. Rosen, "Modified Fresnel computer-generated hologram directly recorded by multiple-viewpoint projections," *Appl. Opt.* **47**, D21–D27 (2008).
41. T. S. Naohisa Okada, Y. Ichihashi, R. Oi, K. Yamamoto, T. Kakue, and T. Ito, "Fast calculation of a computer-generated hologram for RGB and depth images using a wavefront recording plane method," *Photon. Lett. Pol.* **6**, 90–92 (2014).

42. P. Su, W. Cao, J. Ma, B. Cheng, X. Liang, L. Cao, and G. Jin, "Fast computer-generated hologram generation method for three-dimensional point cloud model," *J. Disp. Technol.* **12**, 1688–1694 (2016).
43. S. Jiao, Z. Zhuang, and W. Zou, "Fast computer generated hologram calculation with a mini look-up table incorporated with radial symmetric interpolation," *Opt. Express* **25**, 112–123 (2017).
44. T. Shimobaba, H. Nakayama, N. Masuda, and T. Ito, "Rapid calculation algorithm of Fresnel computer-generated-hologram using look-up table and wavefront-recording plane methods for three-dimensional display," *Opt. Express* **18**, 19504–19509 (2010).
45. R. L. Lucke, "Rayleigh-Sommerfeld diffraction and Poisson's spot," *Eur. J. Phys.* **27**, 193–204 (2006).
46. Lord Rayleigh, "On the passage of waves through apertures in plane screens, and allied problems," *Philos. Mag.* **43**(263), 259–272 (1897).
47. J. W. Cooley and J. W. Tukey, "An algorithm for the machine calculation of complex Fourier series," *Math. Comput.* **19**, 297 (1965).
48. K. Khare, *Fourier Optics and Computational Imaging* (Wiley, 2015).
49. T.-C. Poon and J.-P. Liu, *Introduction to Modern Digital Holography: With MATLAB* (Cambridge University, 2014).
50. J. J. Burch, "A computer algorithm for the synthesis of spatial frequency filters," *Proc. IEEE* **55**, 599–601 (1967).
51. T. S. Huang and B. Prasada, "Considerations on the generation and processing of holograms by digital computers," *MIT/RLE Quar. Prog. Rep.* **81**, 199–205 (1966).
52. M. Makowski, M. Sypek, A. Kolodziejczyk, and G. Mikula, "Three-plane phase-only computer hologram generated with iterative Fresnel algorithm," *Opt. Eng.* **44**, 125805 (2005).
53. K. Choi, H. Kim, and B. Lee, "Synthetic phase holograms for auto-stereoscopic image displays using a modified IFTA," *Opt. Express* **12**, 2454–2462 (2004).
54. S. Kirkpatrick, C. D. Gelatt, and M. P. Vecchi, "Optimization by simulated annealing," *Science* **220**, 671–680 (1983).
55. D. E. Goldberg, *Genetic Algorithms in Search, Optimization and Machine Learning* (Addison-Wesley, 1989).
56. N. Yoshikawa and T. Yatagai, "Phase optimization of a kinoform by simulated annealing," *Appl. Opt.* **33**, 863–868 (1994).
57. H. Li, X. Wan, T. Liu, Z. Liu, and Y. Zhu, "A computed tomography reconstruction algorithm based on multipurpose optimal criterion and simulated annealing theory," *Chin. Opt. Lett.* **5**, 340–343 (2007).
58. C. Chang, J. Xia, L. Yang, W. Lei, Z. Yang, and J. Chen, "Speckle-suppressed phase-only holographic three-dimensional display based on double-constraint Gerchberg-Saxton algorithm," *Appl. Opt.* **54**, 6994–7001 (2015).
59. A. V. Zea, J. F. Barrera Ramirez, and R. Torroba, "Optimized random phase only holograms," *Opt. Lett.* **43**, 731–734 (2018).
60. P. Sun, S. Chang, S. Liu, X. Tao, C. Wang, and Z. Zheng, "Holographic near-eye display system based on double-convergence light Gerchberg-Saxton algorithm," *Opt. Express* **26**, 10140–10151 (2018).
61. R. W. Gerchberg and W. O. Saxton, "A practical algorithm for the determination of phase from image and diffraction plane pictures," *Optik* **35**, 237–246 (1972).
62. G.-Z. Yang, B.-Z. Dong, B.-Y. Gu, J. Y. Zhuang, and O. K. Ersoy, "Gerchberg-Saxton and Yang-Gu algorithms for phase retrieval in a nonunitary transform system: a comparison," *Appl. Opt.* **33**, 209–218 (1994).
63. M.-P. Chang and O. Ersoy, "The modified input-output algorithm for the synthesis of computer-generated holograms," *Optik* **95**, 155–160 (1994).

64. D. Im, J. Cho, J. Hahn, B. Lee, and H. Kim, "Accelerated synthesis algorithm of polygon computer-generated holograms," *Opt. Express* **23**, 2863–2871 (2015).
65. J.-H. Park, "Recent progress in computer-generated holography for three-dimensional scenes," *J. Inf. Disp.* **18**, 1–12 (2016).
66. H. Kim, J. Hahn, and B. Lee, "Mathematical modeling of triangle-mesh-modeled three-dimensional surface objects for digital holography," *Appl. Opt.* **47**, D117–D127 (2008).
67. Y.-P. Zhang, F. Wang, T.-C. Poon, S. Fan, and W. Xu, "Fast generation of full analytical polygon-based computer-generated holograms," *Opt. Express* **26**, 19206–19224 (2018).
68. J. S. Chen and D. P. Chu, "Improved layer-based method for rapid hologram generation and real-time interactive holographic display applications," *Opt. Express* **23**, 18143–18155 (2015).
69. C. Argyropoulos, N. M. Estakhri, F. Monticone, and A. Alù, "Negative refraction, gain and nonlinear effects in hyperbolic metamaterials," *Opt. Express* **21**, 15037–15047 (2013).
70. K. Aydin, I. Bulu, and E. Ozbay, "Subwavelength resolution with a negative-index metamaterial superlens," *Appl. Phys. Lett.* **90**, 254102 (2007).
71. N. I. Zheludev and Y. S. Kivshar, "From metamaterials to metadevices," *Nat. Mater.* **11**, 917–924 (2012).
72. N. Yu and F. Capasso, "Flat optics with designer metasurfaces," *Nat. Mater.* **13**, 139–150 (2014).
73. A. Epstein and G. V. Eleftheriades, "Synthesis of passive lossless metasurfaces using auxiliary fields for reflectionless beam splitting and perfect reflection," *Phys. Rev. Lett.* **117**, 256103 (2016).
74. X. Luo, M. Pu, X. Ma, and X. Li, "Taming the electromagnetic boundaries via metasurfaces: from theory and fabrication to functional devices," *Int. J. Antennas Propag.* **2015**, 204127 (2015).
75. S. Liu, P. P. Vabishchevich, A. Vaskin, J. L. Reno, G. A. Keeler, M. B. Sinclair, I. Staude, and I. Brener, "An all-dielectric metasurface as a broadband optical frequency mixer," *Nat. Commun.* **9**, 2507 (2018).
76. E. Arbabi, J. Li, R. J. Hutchins, S. M. Kamali, A. Arbabi, Y. Horie, P. Van Dorpe, V. Grdinaru, D. A. Wagenaar, and A. Faraon, "Two-photon microscopy with a double-wavelength metasurface objective lens," *Nano Lett.* **18**, 4943–4948 (2018).
77. N. Meinzer, W. L. Barnes, and I. R. Hooper, "Plasmonic meta-atoms and metasurfaces," *Nat. Photonics* **8**, 889–898 (2014).
78. F. Zhou, Y. Liu, and W. Cai, "Plasmonic holographic imaging with V-shaped nanoantenna array," *Opt. Express* **21**, 4348–4354 (2013).
79. N. Yu, P. Genevet, M. A. Kats, F. Aieta, J. P. Tetienne, F. Capasso, and Z. Gaburro, "Light propagation with phase discontinuities: generalized laws of reflection and refraction," *Science* **334**, 333–337 (2011).
80. L. Liu, X. Zhang, Z. Zhao, M. Pu, P. Gao, Y. Luo, J. Jin, C. Wang, and X. Luo, "Batch fabrication of metasurface holograms enabled by plasmonic cavity lithography," *Adv. Opt. Mater.* **5**, 1700429 (2017).
81. M. Khorasaninejad, W. T. Chen, R. C. Devlin, J. Oh, A. Y. Zhu, and F. Capasso, "Metalenses at visible wavelengths: diffraction-limited focusing and subwavelength resolution imaging," *Science* **352**, 1190–1194 (2016).
82. W. T. Chen, A. Y. Zhu, V. Sanjeev, M. Khorasaninejad, Z. Shi, E. Lee, and F. Capasso, "A broadband achromatic metalens for focusing and imaging in the visible," *Nat. Nanotechnol.* **13**, 220–226 (2018).
83. S. Wang, P. C. Wu, V.-C. Su, Y.-C. Lai, M.-K. Chen, H. Y. Kuo, B. H. Chen, Y. H. Chen, T.-T. Huang, J.-H. Wang, R.-M. Lin, C.-H. Kuan, T. Li, Z. Wang,

- S. Zhu, and D. P. Tsai, "A broadband achromatic metasurface in the visible," *Nat. Nanotechnol.* **13**, 227–232 (2018).
84. G.-Y. Lee, J.-Y. Hong, S. Hwang, S. Moon, H. Kang, S. Jeon, H. Kim, J.-H. Jeong, and B. Lee, "Metasurface eyepiece for augmented reality," *Nat. Commun.* **9**, 4562 (2018).
85. S. Li, X. Li, G. Wang, S. Liu, L. Zhang, C. Zeng, L. Wang, Q. Sun, W. Zhao, and W. Zhang, "Multidimensional manipulation of photonic spin Hall effect with a single-layer dielectric metasurface," *Adv. Opt. Mater.* **7**, 1801365 (2019).
86. A. Arbabi, E. Arbabi, S. M. Kamali, Y. Horie, S. Han, and A. Faraon, "Miniature optical planar camera based on a wide-angle metasurface doublet corrected for monochromatic aberrations," *Nat. Commun.* **7**, 13682 (2016).
87. P. K. Jha, X. Ni, C. Wu, Y. Wang, and X. Zhang, "Metasurface-enabled remote quantum interference," *Phys. Rev. Lett.* **115**, 025501 (2015).
88. C. Huang, J. Yang, X. Wu, J. Song, M. Pu, C. Wang, and X. Luo, "Reconfigurable metasurface cloak for dynamical electromagnetic illusions," *ACS Photon.* **5**, 1718–1725 (2018).
89. H. Chu, Q. Li, B. Liu, J. Luo, S. Sun, Z. H. Hang, L. Zhou, and Y. Lai, "A hybrid invisibility cloak based on integration of transparent metasurfaces and zero-index materials," *Light Sci. Appl.* **7**, 50 (2018).
90. C. Wang, Z. Li, M.-H. Kim, X. Xiong, X.-F. Ren, G.-C. Guo, N. Yu, and M. Lončar, "Metasurface-assisted phase-matching-free second harmonic generation in lithium niobate waveguides," *Nat. Commun.* **8**, 2098 (2017).
91. G. Zheng, H. Muhlenbernd, M. Kenney, G. Li, T. Zentgraf, and S. Zhang, "Metasurface holograms reaching 80% efficiency," *Nat. Nanotechnol.* **10**, 308–312 (2015).
92. L. Huang, X. Chen, H. Mühlenbernd, H. Zhang, S. Chen, B. Bai, Q. Tan, G. Jin, K.-W. Cheah, C.-W. Qiu, J. Li, T. Zentgraf, and S. Zhang, "Three-dimensional optical holography using a plasmonic metasurface," *Nat. Commun.* **4**, 2808 (2013).
93. X. Ni, A. V. Kildishev, and V. M. Shalaev, "Metasurface holograms for visible light," *Nat. Commun.* **4**, 2807 (2013).
94. X. Yin, Z. Ye, J. Rho, Y. Wang, and X. Zhang, "Photonic spin Hall effect at metasurfaces," *Science* **339**, 1405–1407 (2013).
95. N. Shitrit, I. Yulevich, E. Maguid, D. Ozeri, D. Veksler, V. Kleiner, and E. Hasman, "Spin-optical metamaterial route to spin-controlled photonics," *Science* **340**, 724–726 (2013).
96. Y. Zhang, W. Liu, J. Gao, and X. Yang, "Generating focused 3D perfect vortex beams by plasmonic metasurfaces," *Adv. Opt. Mater.* **6**, 1701228 (2018).
97. F. Yue, D. Wen, J. Xin, B. D. Gerardot, J. Li, and X. Chen, "Vector vortex beam generation with a single plasmonic metasurface," *ACS Photon.* **3**, 1558–1563 (2016).
98. M. Faraji-Dana, E. Arbabi, A. Arbabi, S. M. Kamali, H. Kwon, and A. Faraon, "Compact folded metasurface spectrometer," *Nat. Commun.* **9**, 4196 (2018).
99. A. Y. Zhu, W.-T. Chen, M. Khorasaninejad, J. Oh, A. Zaidi, I. Mishra, R. C. Devlin, and F. Capasso, "Ultra-compact visible chiral spectrometer with meta-lenses," *APL Photon.* **2**, 036103 (2017).
100. M. Jang, Y. Horie, A. Shibukawa, J. Brake, Y. Liu, S. M. Kamali, A. Arbabi, H. Ruan, A. Faraon, and C. Yang, "Wavefront shaping with disorder-engineered metasurfaces," *Nat. Photonics* **12**, 84–90 (2018).
101. A. E. Minovich, A. E. Miroshnichenko, A. Y. Bykov, T. V. Murzina, D. N. Neshev, and Y. S. Kivshar, "Functional and nonlinear optical metasurfaces," *Laser Photon. Rev.* **9**, 195–213 (2015).

102. H.-H. Hsiao, C. H. Chu, and D. P. Tsai, "Fundamentals and applications of metasurfaces," *Small Methods* **1**, 1600064 (2017).
103. A. I. Kuznetsov, A. E. Miroshnichenko, M. L. Brongersma, Y. S. Kivshar, and B. Luk'yanchuk, "Optically resonant dielectric nanostructures," *Science* **354**, aag2472 (2016).
104. Z.-L. Deng and G. Li, "Metasurface optical holography," *Mater. Today Phys.* **3** (December 2017), 16–32 (2017).
105. W. Wan, J. Gao, and X. Yang, "Metasurface holograms for holographic imaging," *Adv. Opt. Mater.* **5**, 1700541 (2017).
106. S. Sun, K.-Y. Yang, C.-M. Wang, T.-K. Juan, W. T. Chen, C. Y. Liao, Q. He, S. Xiao, W.-T. Kung, G.-Y. Guo, L. Zhou, and D. P. Tsai, "High-efficiency broadband anomalous reflection by gradient meta-surfaces," *Nano Lett.* **12**, 6223–6229 (2012).
107. B. Wang, B. Quan, J. He, Z. Xie, X. Wang, J. Li, Q. Kan, and Y. Zhang, "Wavelength de-multiplexing metasurface hologram," *Sci. Rep.* **6**, 35657 (2016).
108. L. Huang, H. Muhlenbernd, X. Li, X. Song, B. Bai, Y. Wang, and T. Zentgraf, "Broadband hybrid holographic multiplexing with geometric metasurfaces," *Adv. Mater.* **27**, 6444–6449 (2015).
109. W. Luo, S. Sun, H.-X. Xu, Q. He, and L. Zhou, "Transmissive ultrathin Pancharatnam-Berry metasurfaces with nearly 100% efficiency," *Phys. Rev. Appl.* **7**, 044033 (2017).
110. R. C. Devlin, M. Khorasaninejad, W. T. Chen, J. Oh, and F. Capasso, "Broadband high-efficiency dielectric metasurfaces for the visible spectrum," *Proc. Natl. Acad. Sci. USA* **113**, 10473–10478 (2016).
111. X. Li, L. Chen, Y. Li, X. Zhang, M. Pu, Z. Zhao, X. Ma, Y. Wang, M. Hong, and X. Luo, "Multicolor 3D meta-holography by broadband plasmonic modulation," *Sci. Adv.* **2**, e1601102 (2016).
112. W. Zhao, H. Jiang, B. Liu, J. Song, Y. Jiang, C. Tang, and J. Li, "Dielectric Huygens' metasurface for high-efficiency hologram operating in transmission mode," *Sci. Rep.* **6**, 30613 (2016).
113. A. Arbabi, Y. Horie, M. Bagheri, and A. Faraon, "Dielectric metasurfaces for complete control of phase and polarization with subwavelength spatial resolution and high transmission," *Nat. Nanotechnol.* **10**, 937–943 (2015).
114. M. Pu, P. Chen, C. Wang, Y. Wang, Z. Zhao, C. Hu, C. Huang, and X. Luo, "Broadband anomalous reflection based on gradient low-Q meta-surface," *AIP Adv.* **3**, 052136 (2013).
115. C. Pfeiffer and A. Grbic, "Metamaterial Huygens' surfaces: tailoring wave fronts with reflectionless sheets," *Phys. Rev. Lett.* **110**, 197401 (2013).
116. L. Liu, X. Zhang, M. Kenney, X. Su, N. Xu, C. Ouyang, Y. Shi, J. Han, W. Zhang, and S. Zhang, "Broadband metasurfaces with simultaneous control of phase and amplitude," *Adv. Mater.* **26**, 5031–5036 (2014).
117. Q. He, S. Sun, S. Xiao, and L. Zhou, "High-efficiency metasurfaces: principles, realizations, and applications," *Adv. Opt. Mater.* **6**, 1800415 (2018).
118. N. K. Grady, J. E. Heyes, D. R. Chowdhury, Y. Zeng, M. T. Reiten, A. K. Azad, A. J. Taylor, D. A. R. Dalvit, and H.-T. Chen, "Terahertz metamaterials for linear polarization conversion and anomalous refraction," *Science* **340**, 1304–1307 (2013).
119. S. Fan, W. Suh, and J. D. Joannopoulos, "Temporal coupled-mode theory for the Fano resonance in optical resonators," *J. Opt. Soc. Am. A* **20**, 569–572 (2003).
120. J. Anandan, "The geometric phase," *Nature* **360**, 307–313 (1992).
121. X. Luo, "Principles of electromagnetic waves in metasurfaces," *Sci. China Phys. Mech.* **58**, 594201 (2015).

122. K. Li, Y. Guo, M. Pu, X. Li, X. Ma, Z. Zhao, and X. Luo, "Dispersion controlling meta-lens at visible frequency," *Opt. Express* **25**, 21419–21427 (2017).
123. H. Yang, G. Li, G. Cao, F. Yu, Z. Zhao, K. Ou, X. Chen, and W. Lu, "High efficiency dual-wavelength achromatic metalens via cascaded dielectric metasurfaces," *Opt. Mater. Express* **8**, 1940–1950 (2018).
124. A. E. H. Love, "I. The integration of the equations of propagation of electric waves," *Philos. Trans. R. Soc. London A* **197**, 1–45 (1901).
125. Y. F. Yu, A. Y. Zhu, R. Paniagua-Domínguez, Y. H. Fu, B. Luk'yanchuk, and A. I. Kuznetsov, "High-transmission dielectric metasurface with 2π phase control at visible wavelengths," *Laser Photon. Rev.* **9**, 412–418 (2015).
126. M. Kim, A. M. H. Wong, and G. V. Eleftheriades, "Optical Huygens' metasurfaces with independent control of the magnitude and phase of the local reflection coefficients," *Phys. Rev. X* **4**, 041042 (2014).
127. K. E. Chong, I. Staude, A. James, J. Dominguez, S. Liu, S. Campione, G. S. Subramania, T. S. Luk, M. Decker, D. N. Neshev, I. Brener, and Y. S. Kivshar, "Polarization-independent silicon metadevices for efficient optical wavefront control," *Nano Lett.* **15**, 5369–5374 (2015).
128. M. Decker, I. Staude, M. Falkner, J. Dominguez, D. N. Neshev, I. Brener, T. Pertsch, and Y. S. Kivshar, "High-efficiency dielectric Huygens' surfaces," *Adv. Opt. Mater.* **3**, 813–820 (2015).
129. D. Lin, P. Fan, E. Hasman, and M. L. Brongersma, "Dielectric gradient metasurface optical elements," *Science* **345**, 298–302 (2014).
130. M. Khorasaninejad, A. Y. Zhu, C. Roques-Carmes, W. T. Chen, J. Oh, I. Mishra, R. C. Devlin, and F. Capasso, "Polarization-insensitive metalenses at visible wavelengths," *Nano Lett.* **16**, 7229–7234 (2016).
131. T. Xu, C. Du, C. Wang, and X. Luo, "Subwavelength imaging by metallic slab lens with nanoslits," *Appl. Phys. Lett.* **91**, 201501 (2007).
132. Y. Liang, H. Liu, F. Wang, H. Meng, J. Guo, J. Li, and Z. Wei, "High-efficiency, near-diffraction limited, dielectric metasurface lenses based on crystalline titanium dioxide at visible wavelengths," *Nanomaterials (Basel)* **8**, 288 (2018).
133. A. Arbabi, Y. Horie, A. J. Ball, M. Bagheri, and A. Faraon, "Subwavelength-thick lenses with high numerical apertures and large efficiency based on high-contrast transmitarrays," *Nat. Commun.* **6**, 7069 (2015).
134. Y. Yifat, M. Eitan, Z. Iluz, Y. Hanein, A. Boag, and J. Scheuer, "Highly efficient and broadband wide-angle holography using patch-dipole nanoantenna reflectarrays," *Nano Lett.* **14**, 2485–2490 (2014).
135. S. Sun, Q. He, S. Xiao, Q. Xu, X. Li, and L. Zhou, "Gradient-index metasurfaces as a bridge linking propagating waves and surface waves," *Nat. Mater.* **11**, 426–431 (2012).
136. L. Wang, S. Kruk, K. Koshelev, I. Kravchenko, B. Luther-Davies, and Y. Kivshar, "Nonlinear wavefront control with all-dielectric metasurfaces," *Nano Lett.* **18**, 3978–3984 (2018).
137. A. Krasnok, M. Tymchenko, and A. Alù, "Nonlinear metasurfaces: a paradigm shift in nonlinear optics," *Mater. Today* **21**(1), 8–21 (2018).
138. S. Keren-Zur, L. Michaeli, H. Suchowski, and T. Ellenbogen, "Shaping light with nonlinear metasurfaces," *Adv. Opt. Photon.* **10**, 309–353 (2018).
139. G. Li, S. Zhang, and T. Zentgraf, "Nonlinear photonic metasurfaces," *Nat. Rev. Mater.* **2**, 17010 (2017).
140. L. Huang, S. Zhang, and T. Zentgraf, "Metasurface holography: from fundamentals to applications," *Nanophotonics* **7**, 1169–1190 (2018).
141. P. Genevet and F. Capasso, "Holographic optical metasurfaces: a review of current progress," *Rep. Prog. Phys.* **78**, 024401 (2015).

142. A. Martins, J. Li, A. F. da Mota, Y. Wang, L. G. Neto, J. P. do Carmo, F. L. Teixeira, E. R. Martins, and B. V. Borges, "Highly efficient holograms based on c-Si metasurfaces in the visible range," *Opt. Express* **26**, 9573–9583 (2018).
143. G. Yoon, D. Lee, K. T. Nam, and J. Rho, "Pragmatic metasurface hologram at visible wavelength: the balance between diffraction efficiency and fabrication compatibility," *ACS Photon.* **5**, 1643–1647 (2017).
144. K. Huang, H. Liu, F. J. Garcia-Vidal, M. Hong, B. Luk'yanchuk, J. Teng, and C.-W. Qiu, "Ultrahigh-capacity non-periodic photon sieves operating in visible light," *Nat. Commun.* **6**, 7059 (2015).
145. X. Zhang, X. Li, J. Jin, M. Pu, X. Ma, J. Luo, Y. Guo, C. Wang, and X. Luo, "Polarization-independent broadband meta-holograms via polarization-dependent nanoholes," *Nanoscale* **10**, 9304–9310 (2018).
146. K. Huang, Z. Dong, S. Mei, L. Zhang, Y. Liu, H. Liu, H. Zhu, J. Teng, B. Luk'yanchuk, J. K. W. Yang, and C.-W. Qiu, "Silicon multi-meta-holograms for the broadband visible light," *Laser Photon. Rev.* **10**, 500–509 (2016).
147. Q. T. Li, F. Dong, B. Wang, F. Gan, J. Chen, Z. Song, L. Xu, W. Chu, Y. F. Xiao, Q. Gong, and Y. Li, "Polarization-independent and high-efficiency dielectric metasurfaces for visible light," *Opt. Express* **24**, 16309–16319 (2016).
148. Q. Wei, L. Huang, X. Li, J. Liu, and Y. Wang, "Broadband multiplane holography based on plasmonic metasurface," *Adv. Opt. Mater.* **5**, 1700434 (2017).
149. M. Khorasaninejad, A. Ambrosio, P. Kanhaiya, and F. Capasso, "Broadband and chiral binary dielectric meta-holograms," *Sci. Adv.* **2**, e1501258 (2016).
150. K. E. Chong, L. Wang, I. Staude, A. R. James, J. Dominguez, S. Liu, G. S. Subramania, M. Decker, D. N. Neshev, I. Brener, and Y. S. Kivshar, "Efficient polarization-insensitive complex wavefront control using Huygens' metasurfaces based on dielectric resonant meta-atoms," *ACS Photon.* **3**, 514–519 (2016).
151. L. Wang, S. Kruk, H. Tang, T. Li, I. Kravchenko, D. N. Neshev, and Y. S. Kivshar, "Grayscale transparent metasurface holograms," *Optica* **3**, 1504–1505 (2016).
152. S. M. Kamali, E. Arbabi, A. Arbabi, Y. Horie, M. Faraji-Dana, and A. Faraon, "Angle-multiplexed metasurfaces: encoding independent wavefronts in a single metasurface under different illumination angles," *Phys. Rev. X* **7**, 041056 (2017).
153. Z. Li, I. Kim, L. Zhang, M. Q. Mehmood, M. S. Anwar, M. Saleem, D. Lee, K. T. Nam, S. Zhang, B. Luk'yanchuk, Y. Wang, G. Zheng, J. Rho, and C.-W. Qiu, "Dielectric meta-holograms enabled with dual magnetic resonances in visible light," *ACS Nano* **11**, 9382–9389 (2017).
154. W. T. Chen, K.-Y. Yang, C.-M. Wang, Y.-W. Huang, G. Sun, I. D. Chiang, C. Y. Liao, W.-L. Hsu, H. T. Lin, S. Sun, L. Zhou, A. Q. Liu, and D. P. Tsai, "High-efficiency broadband meta-hologram with polarization-controlled dual images," *Nano Lett.* **14**, 225–230 (2014).
155. Y. Montelongo, J. O. Tenorio-Pearl, W. I. Milne, and T. D. Wilkinson, "Polarization switchable diffraction based on subwavelength plasmonic nanoantennas," *Nano Lett.* **14**, 294–298 (2014).
156. D. Wen, F. Yue, G. Li, G. Zheng, K. Chan, S. Chen, M. Chen, K. F. Li, P. W. Wong, K. W. Cheah, E. Y. Pun, S. Zhang, and X. Chen, "Helicity multiplexed broadband metasurface holograms," *Nat. Commun.* **6**, 8241 (2015).
157. J. P. Balthasar Mueller, N. A. Rubin, R. C. Devlin, B. Groever, and F. Capasso, "Metasurface polarization optics: independent phase control of arbitrary orthogonal states of polarization," *Phys. Rev. Lett.* **118**, 113901 (2017).
158. C. Zhang, F. Yue, D. Wen, M. Chen, Z. Zhang, W. Wang, and X. Chen, "Multichannel metasurface for simultaneous control of holograms and twisted light beams," *ACS Photon.* **4**, 1906–1912 (2017).

159. J. Burch, D. Wen, X. Chen, and A. Di Falco, "Conformable holographic metasurfaces," *Sci. Rep.* **7**, 4520 (2017).
160. J. Burch and A. Di Falco, "Holography using curved metasurfaces," *Photonics* **6**, 8 (2019).
161. Y.-W. Huang, W. T. Chen, W.-Y. Tsai, P. C. Wu, C.-M. Wang, G. Sun, and D. P. Tsai, "Aluminum plasmonic multicolor meta-hologram," *Nano Lett.* **15**, 3122–3127 (2015).
162. B. Wang, F. Dong, Q.-T. Li, D. Yang, C. Sun, J. Chen, Z. Song, L. Xu, W. Chu, Y.-F. Xiao, Q. Gong, and Y. Li, "Visible-frequency dielectric metasurfaces for multiwavelength achromatic and highly dispersive holograms," *Nano Lett.* **16**, 5235–5240 (2016).
163. W. Zhao, B. Liu, H. Jiang, J. Song, Y. Pei, and Y. Jiang, "Full-color hologram using spatial multiplexing of dielectric metasurface," *Opt. Lett.* **41**, 147–150 (2016).
164. F. F. Qin, Z. Z. Liu, Z. Zhang, Q. Zhang, and J. J. Xiao, "Broadband full-color multichannel hologram with geometric metasurface," *Opt. Express* **26**, 11577–11586 (2018).
165. W. Wan, J. Gao, and X. Yang, "Full-color plasmonic metasurface holograms," *ACS Nano* **10**, 10671–10680 (2016).
166. B. Lee, "Metasurface holograms webinar," in *OSA Holography and Diffractive Optics Technical Group* (Optical Society of America, 2018).
167. S. Sun, W. Yang, C. Zhang, J. Jing, Y. Gao, X. Yu, Q. Song, and S. Xiao, "Real-time tunable colors from microfluidic reconfigurable all-dielectric metasurfaces," *ACS Nano* **12**, 2151–2159 (2018).
168. Q. Wang, X. Zhang, Y. Xu, J. Gu, Y. Li, Z. Tian, R. Singh, S. Zhang, J. Han, and W. Zhang, "Broadband metasurface holograms: toward complete phase and amplitude engineering," *Sci. Rep.* **6**, 32867 (2016).
169. S. L. Jia, X. Wan, P. Su, Y. J. Zhao, and T. J. Cui, "Broadband metasurface for independent control of reflected amplitude and phase," *AIP Adv.* **6**, 045024 (2016).
170. G. Y. Lee, G. Yoon, S. Y. Lee, H. Yun, J. Cho, K. Lee, H. Kim, J. Rho, and B. Lee, "Complete amplitude and phase control of light using broadband holographic metasurfaces," *Nanoscale* **10**, 4237–4245 (2018).
171. X. Song, L. Huang, C. Tang, J. Li, X. Li, J. Liu, Y. Wang, and T. Zentgraf, "Selective diffraction with complex amplitude modulation by dielectric metasurfaces," *Adv. Opt. Mater.* **6**, 1701181 (2018).
172. Q. Jiang, Z. He, G. Jin, and L. Cao, "Complex amplitude modulation metasurface with dual resonance in transmission mode," *Proc. SPIE* **10944**, 109440A (2019).
173. M. Tymchenko, J. S. Gomez-Diaz, J. Lee, N. Nookala, M. A. Belkin, and A. Alù, "Advanced control of nonlinear beams with Pancharatnam-Berry metasurfaces," *Phys. Rev. B* **94**, 214303 (2016).
174. G. Li, S. Chen, N. Pholchai, B. Reineke, P. W. H. Wong, E. Y. B. Pun, K. W. Cheah, T. Zentgraf, and S. Zhang, "Continuous control of the nonlinearity phase for harmonic generations," *Nat. Mater.* **14**, 607–612 (2015).
175. W. Ye, F. Zeuner, X. Li, B. Reineke, S. He, C.-W. Qiu, J. Liu, Y. Wang, S. Zhang, and T. Zentgraf, "Spin and wavelength multiplexed nonlinear metasurface holography," *Nat. Commun.* **7**, 11930 (2016).
176. E. Almeida, O. Bitton, and Y. Prior, "Nonlinear metamaterials for holography," *Nat. Commun.* **7**, 12533 (2016).
177. T. Cui, B. Bai, and H.-B. Sun, "Tunable metasurfaces based on active materials," *Adv. Funct. Mater.* **29**, 1806692 (2019).

178. A.-K. U. Michel, D. N. Chigrin, T. W. W. Maß, K. Schönauer, M. Salinga, M. Wuttig, and T. Taubner, "Using low-loss phase-change materials for mid-infrared antenna resonance tuning," *Nano Lett.* **13**, 3470–3475 (2013).
179. A. V. Pogrebnyakov, J. A. Bossard, J. P. Turpin, J. D. Musgraves, H. J. Shin, C. Rivero-Baleine, N. Podraza, K. A. Richardson, D. H. Werner, and T. S. Mayer, "Reconfigurable near-IR metasurface based on $\text{Ge}_2\text{Sb}_2\text{Te}_5$ phase-change material," *Opt. Mater. Express* **8**, 2264–2275 (2018).
180. Y. Chen, X. Li, Y. Sonnefraud, A. I. Fernández-Domínguez, X. Luo, M. Hong, and S. A. Maier, "Engineering the phase front of light with phase-change material based planar lenses," *Sci. Rep.* **5**, 8660 (2015).
181. L. Wang, W. Hong, L. Deng, S. Li, C. Zhang, J. Zhu, and H. Wang, "Reconfigurable multifunctional metasurface hybridized with vanadium dioxide at terahertz frequencies," *Materials* **11**, 2040 (2018).
182. S.-Y. Lee, Y.-H. Kim, S.-M. Cho, G. H. Kim, T.-Y. Kim, H. Ryu, H. N. Kim, H. B. Kang, C.-Y. Hwang, and C.-S. Hwang, "Holographic image generation with a thin-film resonance caused by chalcogenide phase-change material," *Sci. Rep.* **7**, 41152 (2017).
183. M. T. Nouman, J. Hwang, M. Faiyaz, G. Lee, D.-Y. Noh, and J.-H. Jang, "Dynamic-metasurface-based cavity structures for enhanced absorption and phase modulation," *ACS Photon.* **6**, 374–381 (2018).
184. C. H. Chu, M. L. Tseng, J. Chen, P. C. Wu, Y.-H. Chen, H.-C. Wang, T.-Y. Chen, W. T. Hsieh, H. J. Wu, G. Sun, and D. P. Tsai, "Active dielectric metasurface based on phase-change medium," *Laser Photon. Rev.* **10**, 986–994 (2016).
185. X. Liu, Q. Wang, X. Zhang, H. Li, Q. Xu, Y. Xu, X. Chen, S. Li, M. Liu, Z. Tian, C. Zhang, C. Zou, J. Han, and W. Zhang, "Thermally dependent dynamic metaholography using a vanadium dioxide integrated metasurface," *Adv. Opt. Mater.* (to be published).
186. Z. Miao, Q. Wu, X. Li, Q. He, K. Ding, Z. An, Y. Zhang, and L. Zhou, "Widely tunable terahertz phase modulation with gate-controlled graphene metasurfaces," *Phys. Rev. X* **5**, 041027 (2015).
187. P. C. Wu, N. Papasimakis, and D. P. Tsai, "Self-affine graphene metasurfaces for tunable broadband absorption," *Phys. Rev. Appl.* **6**, 044019 (2016).
188. W. Yao, L. Tang, J. Wang, C. Ji, X. Wei, and Y. Jiang, "Spectrally and spatially tunable terahertz metasurface lens based on graphene surface plasmons," *IEEE Photon. J.* **10**, 4800909 (2018).
189. M. Xu, T. Liang, M. Shi, and H. Chen, "Graphene-like two-dimensional materials," *Chem. Rev.* **113**, 3766–3798 (2013).
190. N. Dabidian, I. Kholmanov, A. B. Khanikaev, K. Tatar, S. Trendafilov, S. H. Mousavi, C. Magnuson, R. S. Ruoff, and G. Shvets, "Electrical switching of infrared light using graphene integration with plasmonic Fano resonant metasurfaces," *ACS Photon.* **2**, 216–227 (2015).
191. L. Li, T. Jun Cui, W. Ji, S. Liu, J. Ding, X. Wan, Y. Bo Li, M. Jiang, C. W. Qiu, and S. Zhang, "Electromagnetic reprogrammable coding-metasurface holograms," *Nat. Commun.* **8**, 197 (2017).
192. K. Chen, Y. Feng, F. Monticone, J. Zhao, B. Zhu, T. Jiang, L. Zhang, Y. Kim, X. Ding, S. Zhang, A. Alù, and C.-W. Qiu, "A reconfigurable active Huygens' metalens," *Adv. Mater.* **29**, 1606422 (2017).
193. P. C. Wu, W. Zhu, Z. X. Shen, P. H. J. Chong, W. Ser, D. P. Tsai, and A.-Q. Liu, "Broadband wide-angle multifunctional polarization converter via liquid-metal-based metasurface," *Adv. Opt. Mater.* **5**, 1600938 (2017).
194. J. Chen, K. Wang, H. Long, X. Han, H. Hu, W. Liu, B. Wang, and P. Lu, "Tungsten disulfide-gold nanohole hybrid metasurfaces for nonlinear metalenses in the visible region," *Nano Lett.* **18**, 1344–1350 (2018).

195. T. Cao, Y. Li, X. Zhang, and Y. Zou, "Theoretical study of tunable chirality from graphene integrated achiral metasurfaces," *Photon. Res.* **5**, 441–449 (2017).
196. Y. C. Jun, J. Reno, T. Ribaudo, E. Shaner, J. J. Greffet, S. Vassant, F. Marquier, M. Sinclair, and I. Brener, "Epsilon-near-zero strong coupling in metamaterial-semiconductor hybrid structures," *Nano Lett.* **13**, 5391–5396 (2013).
197. G. Kafaie Shirmanesh, R. Sokhoyan, R. A. Pala, and H. A. Atwater, "Dual-gated active metasurface at 1550 nm with wide (>300°) phase tunability," *Nano Lett.* **18**, 2957–2963 (2018).
198. T. Lewi, H. A. Evans, N. A. Butakov, and J. A. Schuller, "Ultrawide thermo-optic tuning of PbTe meta-atoms," *Nano Lett.* **17**, 3940–3945 (2017).
199. J. Sautter, I. Staude, M. Decker, E. Rusak, D. N. Neshev, I. Brener, and Y. S. Kivshar, "Active tuning of all-dielectric metasurfaces," *ACS Nano* **9**, 4308–4315 (2015).
200. J. Kobashi, H. Yoshida, and M. Ozaki, "Planar optics with patterned chiral liquid crystals," *Nat. Photonics* **10**, 389–392 (2016).
201. J. Y. Ou, E. Plum, J. Zhang, and N. I. Zheludev, "An electromechanically reconfigurable plasmonic metamaterial operating in the near-infrared," *Nat. Nanotechnol.* **8**, 252–255 (2013).
202. J. Valente, J. Y. Ou, E. Plum, I. J. Youngs, and N. I. Zheludev, "A magneto-electro-optical effect in a plasmonic nanowire material," *Nat. Commun.* **6**, 7021 (2015).
203. A. Howes, W. Wang, I. Kravchenko, and J. Valentine, "Dynamic transmission control based on all-dielectric Huygens metasurfaces," *Optica* **5**, 787–792 (2018).
204. K. Thyagarajan, R. Sokhoyan, L. Zornberg, and H. A. Atwater, "Millivolt modulation of plasmonic metasurface optical response via ionic conductance," *Adv. Mater.* **29**, 1701044 (2017).
205. K. Dong, S. Hong, Y. Deng, H. Ma, J. Li, X. Wang, J. Yeo, L. Wang, S. Lou, K. B. Tom, K. Liu, Z. You, Y. Wei, C. P. Grigoropoulos, J. Yao, and J. Wu, "A lithography-free and field-programmable photonic metacanvas," *Adv. Mater.* **30**, 1703878 (2017).
206. X. Li, H. Ren, X. Chen, J. Liu, Q. Li, C. Li, G. Xue, J. Jia, L. Cao, A. Sahu, B. Hu, Y. Wang, G. Jin, and M. Gu, "A thermally photoreduced graphene oxides for three-dimensional holographic images," *Nat. Commun.* **6**, 6984 (2015).
207. Y. Zhao, Y. Zhang, Q. Shi, S. Liang, W. Huang, W. Kou, and Z. Yang, "Dynamic photoinduced controlling of the large phase shift of terahertz waves via vanadium dioxide coupling nanostructures," *ACS Photon.* **5**, 3040–3050 (2018).
208. J. Guo, T. Wang, H. Zhao, X. Wang, S. Feng, P. Han, W. Sun, J. Ye, G. Situ, H.-T. Chen, and Y. Zhang, "Reconfigurable terahertz metasurface pure phase holograms," *Adv. Opt. Mater.* **7**, 1801696 (2019).
209. X. G. Zhang, W. X. Tang, W. X. Jiang, G. D. Bai, J. Tang, L. Bai, C.-W. Qiu, and T. J. Cui, "Light-controllable digital coding metasurfaces," *Adv. Sci.* **5**, 1801028 (2018).
210. S. C. Malek, H.-S. Ee, and R. Agarwal, "Strain multiplexed metasurface holograms on a stretchable substrate," *Nano Lett.* **17**, 3641–3645 (2017).
211. Y. Lee, S.-J. Kim, J.-G. Yun, C. Kim, S.-Y. Lee, and B. Lee, "Electrically tunable multifunctional metasurface for integrating phase and amplitude modulation based on hyperbolic metamaterial substrate," *Opt. Express* **26**, 32063–32073 (2018).
212. E. Arbabi, A. Arbabi, S. M. Kamali, Y. Horie, M. Faraji-Dana, and A. Faraon, "MEMS-tunable dielectric metasurface lens," *Nat. Commun.* **9**, 812 (2018).

213. S. Kruk, F. Ferreira, N. Mac Suibhne, C. Tsekrekos, I. Kravchenko, A. Ellis, D. Neshev, S. Turitsyn, and Y. Kivshar, "Transparent dielectric metasurfaces for spatial mode multiplexing," *Laser Photon. Rev.* **12**, 1800031 (2018).
214. Y. Li, X. Li, L. Chen, M. Pu, J. Jin, M. Hong, and X. Luo, "Orbital angular momentum multiplexing and demultiplexing by a single metasurface," *Adv. Opt. Mater.* **5**, 1600502 (2017).
215. L. Jin, Z. Dong, S. Mei, Y. F. Yu, Z. Wei, Z. Pan, S. D. Rezaei, X. Li, A. I. Kuznetsov, Y. S. Kivshar, J. K. W. Yang, and C.-W. Qiu, "Noninterleaved metasurface for (2⁶-1) spin- and wavelength-encoded holograms," *Nano Lett.* **18**, 8016–8024 (2018).
216. F. Dong, H. Feng, L. Xu, B. Wang, Z. Song, X. Zhang, L. Yan, X. Li, Y. Tian, W. Wang, L. Sun, Y. Li, and W. Chu, "Information encoding with optical dielectric metasurface via independent multichannels," *ACS Photon.* **6**, 230–237 (2019).
217. G.-Y. Lee, J. Sung, and B. Lee, "Recent advances in metasurface hologram technologies," *ETRI J.* **41**, 10–22 (2019).
218. S. Lan, X. Zhang, M. Taghinejad, S. Rodrigues, K.-T. Lee, Z. Liu, and W. Cai, "Metasurfaces for near-eye augmented reality," *ACS Photon.* **6**, 864–870 (2019).
219. H.-C. Liu, B. Yang, Q. Guo, J. Shi, C. Guan, G. Zheng, H. Mühlenernd, G. Li, T. Zentgraf, and S. Zhang, "Single-pixel computational ghost imaging with helicity-dependent metasurface hologram," *Sci. Adv.* **3**, e1701477 (2017).
220. J. Li, S. Kamin, G. Zheng, F. Neubrech, S. Zhang, and N. Liu, "Addressable metasurfaces for dynamic holography and optical information encryption," *Sci. Adv.* **4**, eaar6768 (2018).
221. N. Verrier and M. Atlan, "Absolute measurement of small-amplitude vibrations by time-averaged heterodyne holography with a dual local oscillator," *Opt. Lett.* **38**, 739–741 (2013).
222. R. Ahmed, A. K. Yetisen, S. H. Yun, and H. Butt, "Color-selective holographic retroreflector array for sensing applications," *Light Sci. Appl.* **6**, e16214 (2017).
223. Y. Lee, S.-J. Kim, H. Park, and B. Lee, "Metamaterials and metasurfaces for sensor applications," *Sensors (Basel)* **17**, 1726 (2017).
224. M. Papaioannou, E. Plum, and N. I. Zheludev, "All-optical pattern recognition and image processing on a metamaterial beam splitter," *ACS Photon.* **4**, 217–222 (2017).
225. W. Ma, F. Cheng, and Y. Liu, "Deep-learning-enabled on-demand design of chiral metamaterials," *ACS Nano* **12**, 6326–6334 (2018).
226. I. Malkiel, M. Mrejen, A. Nagler, U. Arieli, L. Wolf, and H. Suchowski, "Plasmonic nanostructure design and characterization via deep learning," *Light Sci. Appl.* **7**, 60 (2018).
227. Q. Zhang, C. Liu, X. Wan, L. Zhang, S. Liu, Y. Yang, and T. J. Cui, "Machine-learning designs of anisotropic digital coding metasurfaces," *Adv. Theory Simul.* **2**, 1800132 (2019).
228. Z. Liu, D. Zhu, S. P. Rodrigues, K.-T. Lee, and W. Cai, "Generative model for the inverse design of metasurfaces," *Nano Lett.* **18**, 6570–6576 (2018).



Qiang Jiang is a postdoctoral researcher at the Department of Precision Instruments of Tsinghua University in China. He obtained a B.Sc. degree in Applied Physics in 2011 and a Ph.D. degree in Optical Engineering in 2017. He is focusing on the research of metamaterials, holography, and nano-optics. He has published more than 20 papers in reviewed journals and conferences.



Guofan Jin is a professor at the Department of Precision Instruments of Tsinghua University in China. His research interests are in holography and optical information processing. He has published more than 300 papers in reviewed journals and conferences. He is a Chinese Academician of Engineering and a fellow of both The Optical Society (OSA) and SPIE.



Liangcai Cao is an associate professor at the Department of Precision Instruments of Tsinghua University in China. His research interests are in holography and optical information processing. He has published more than 100 papers in reviewed journals and conferences. He is a fellow of SPIE and a senior member of The Optical Society (OSA).